

**MICROSTRIP POST PRODUCTION TUNING BAR ERROR AND
COMPACT RESONATORS USING NEGATIVE REFRACTIVE
INDEX METAMATERIALS**

A Thesis

by

AARON DAVID SCHER

Submitted to the Office of Graduate Studies of
Texas A&M University
in partial fulfillment of the requirements for the degree of
MASTER OF SCIENCE

May 2005

Major Subject: Electrical Engineering

**MICROSTRIP POST PRODUCTION TUNING BAR ERROR AND
COMPACT RESONATORS USING NEGATIVE REFRACTIVE
INDEX METAMATERIALS**

A Thesis

by

AARON DAVID SCHER

Submitted to the Office of Graduate Studies of
Texas A&M University
in partial fulfillment of the requirements for the degree of

MASTER OF SCIENCE

Approved as to style and content by:

Kai Chang
(Chair of Committee)

Krzysztof Michalski
(Member)

Henry Taylor
(Member)

Wayne Saslow
(Member)

Chanan Singh
(Head of Department)

May 2005

Major Subject: Electrical Engineering

ABSTRACT

Microstrip Post Production Tuning Bar Error and Compact Resonators
Using Negative Refractive Index Metamaterials. (May 2005)

Aaron David Scher, B.S., Texas A&M University
Chair of Advisory Committee: Dr. Kai Chang

In this thesis, two separate research topics are undertaken both in the general area of compact RF/microwave circuit design. The first topic involves characterizing the parasitic effects and error due to unused post-production tuning bars. Such tuning bars are used in microwave circuit designs to allow the impedance or length of a microstrip line to be adjusted after fabrication. In general, the tuning bars are simply patterns of small, isolated sections of conductor adjacent to the thru line. Changing the impedance or length of the thru line involves bonding the appropriate tuning bars to the line. Unneeded tuning bars are simply not removed and left isolated. Ideally, there should be no coupling between these unused tuning bars and the thru line. Therefore, the unused tuning bars should have a negligible effect on the circuit's overall performance. To nullify the parasitic effects of the tuning bars, conventional wisdom suggests placing the bars 1.0 to 1.5 substrate heights away from the main line. While successful in the past, this practice may not result in the most efficient and cost-effective placement of tuning bars in today's compact microwave circuits. This thesis facilitates the design of compact tuning bar configurations with minimum parasitic effects by analyzing the error attributable to various common tuning bar configurations with a range of parameters and offset distances. The error is primarily determined through electromagnetic simulations, and the accuracy of these simulations is verified by experimental results. The second topic in this thesis involves the design of compact microwave resonators using the transmission line approach to create negative refractive index metamaterials. A survey of the major developments and fundamental concepts related to negative refractive index technology (with focus on the transmission line approach) is given. Following is the

design and measurement of the compact resonators. The resonators are also compared to their conventional counterparts to demonstrate both compactness and harmonic suppression.

In Memory of
Marian Scher
1953-1986

ACKNOWLEDGEMENTS

I wish to thank Dr. Chang for his continuous help and guidance throughout my work on my masters degree. I would also like to thank Dr. Michalski, Dr. Taylor, and Dr. Saslow for serving as members on my thesis committee. I also thank Mr. Li for his fabrication and technical assistance. Next, I would like to thank Raytheon Co., Electronic Systems Division for their support of this research. The constant encouragement and suggestions of S.P. McFarlane and J.L. Klein are acknowledged. Finally, I wish to express my deep appreciation to my family for all their love and support.

TABLE OF CONTENTS

	Page
ABSTRACT	iii
DEDICATION.....	v
ACKNOWLEDGEMENTS	vi
TABLE OF CONTENTS	vii
LIST OF TABLES	ix
LIST OF FIGURES	x
 CHAPTER	
I INTRODUCTION.....	1
II POST PRODUCTION TUNING BAR ERROR IN MICROWAVE CIRCUITS.....	3
A. Introduction	3
1. Statement of Work.....	3
2. Objectives.....	3
3. Simulation and CAD Software.....	4
4. Research Methods and Approach.....	4
5. Summary	5
B. GaAs MMIC Tuning Bar Configuration	5
1. Matched Load.....	8
2. Mismatched Load.....	10
3. Resonant Frequency Error Analysis.....	15
4. Equivalent Circuit	17
5. U-Shaped Tuning Bars	20
6. Conclusions	24
C. Thin Film Network Tuning Bar Configurations	24
1. Line-Lengthening Tuning Stub Configuration.....	25
2. 6×16 mil Rectangular Tuning Chips in a Cluster (RTCC)..	30
3. 10×10 mil ² RTCC.....	39
4. Mismatched Lines with High VSWR.....	47
5. Conclusions	47

CHAPTER	Page
D. Measurements and Experimental Validation	48
1. Circuit Layout	48
2. Measurements.....	49
3. Conclusions	52
E. Recommendations and Conclusions	52
1. Summary	52
2. Recommendations	54
 III COMPACT RESONATORS USING THE TRANSMISSION LINE APPROACH OF NEGATIVE REFRACTIVE INDEX METAMATERIALS	58
A. Introduction	58
B. The Transmission Line Approach to NRI Metamaterials	61
C. Compact Zeroth-Order Resonators Using NRI Microstrip Line .	67
1. Line Resonators	68
2. Ring Resonators	71
C. Conclusions	74
 IV SUMMARY AND RECOMMENDATIONS FOR FUTURE STUDY	75
A. Summary	75
B. Recommendations for Future Study	76
 REFERENCES.....	77
 APPENDIX A MATLAB CODE FOR GENERATING NRI TL DISPERSION DIAGRAM.....	81
 VITA	84

LIST OF TABLES

TABLE		Page
1	Simulated GaAs tuning bar error results for three important cases. Errors are for matched load (VSWR=1).	9
2	Simulated GaAs quarter wave stub resonant frequency error results for three important cases.	17
3	Simulated line-lengthening tuning stub error results for three important cases.	27
4	Simulated TFN quarter wave stub resonant frequency error results for three important cases.	30
5	Recommended GaAs MMIC tuning bar offset distances.	55
6	Recommended TFN line-lengthening tuning stub offset distances.	56
7	Recommended TFN rectangular tuning chip configuration offset distances.	57

LIST OF FIGURES

FIGURE	Page
1	(a) Top and (b) side view of rectangular GaAs MMIC tuning bar configuration 6
2	Simulated GaAs MMIC (a) rectangular tuning bar configuration and (b) reference thru line 7
3	ADS optimization screenshot 11
4	Maximum (a) Z_{in} , (b) $ S_{21} $ magnitude, and (c) $ S_{21} $ phase error factors. $Z_0 = 50 \Omega$, $L = 200 \mu\text{m}$, substrate thickness = $100 \mu\text{m}$, and $VSWR = 2$ 12
5	Maximum (a) Z_{in} , (b) $ S_{21} $ magnitude, and (c) $ S_{21} $ phase error factors. $Z_0 = 25 \Omega$, $L = 200 \mu\text{m}$, substrate thickness = $100 \mu\text{m}$, and $VSWR = 2$ 13
6	Maximum Z_{in} error factors for (a) $L = 100 \mu\text{m}$ and (b) $L = 150 \mu\text{m}$. Substrate thickness = $100 \mu\text{m}$, $Z_0 = 50 \Omega$, and $VSWR = 2$ 14
7	Maximum Z_{in} error factor for (a) $L = 100 \mu\text{m}$ and (b) $L = 150 \mu\text{m}$. Substrate thickness = $100 \mu\text{m}$, $Z_0 = 25 \Omega$, and $VSWR = 2$ 15
8	GaAs MMIC quarter wave stub resonant circuit at (a) 10 GHz and (b) 35 GHz with rectangular tuning bar. 16
9	Tuning bar configuration. (a) coupled line section representation and (b) equivalent circuit 19
10	GaAs MMIC U-shaped tuning bar configuration. 21
11	Maximum (a) Z_{in} , (b) $ S_{21} $ magnitude, and (c) $ S_{21} $ phase error factors for U-shaped tuning bar. $Z_0 = 50 \Omega$, substrate thickness = $100 \mu\text{m}$, $L_{\text{path}} = 267 \mu\text{m}$, and $VSWR = 2$ 22
12	Maximum (a) Z_{in} , (b) $ S_{21} $ magnitude, and (c) $ S_{21} $ phase error factors for U-shaped tuning bar. $Z_0 = 25 \Omega$, substrate thickness = $100 \mu\text{m}$, $L_{\text{path}} = 560 \mu\text{m}$, and $VSWR = 2$ 23
13	Typical TFN line-lengthening tuning stub geometry 25

FIGURE	Page
14 Simulated TFN (a) line-lengthening tuning stub configuration and (b) reference thru line after de-embedding.....	25
15 Simulated worst-case Z_{in} error factors for (a) alumina and (b) Ferro A6M for one, two, four, and eight line-lengthening stubs.	26
16 Simulated error factors for (a) alumina and (b) Ferro A6M. Substrate thickness = 10 mils.....	28
17 Quarter wave stub resonant circuit at (a) 10 GHz and (b) 35 GHz with line-lengthening tuning stubs	29
18 Typical 6×16 mil ² TFN RTCC configuration.....	31
19 Geometry of 6×16 mil ² RTCC configuration analyzed in this report.	32
20 Simulated (a) Z_{in} , (b) S21 magnitude, and (c) S21 phase error factors for alumina. Results are for 6×16 mil ² tuning bars arranged in five columns on both sides of the line with $d_1 = 5$ mils, $d_2 = 10$ mils, and VSWR = 1...	33
21 Simulated maximum (a) Z_{in} , (b) S21 magnitude, and (c) S21 phase error factors for alumina. Results are for 6×16 mil ² tuning bars arranged as one row-by-five columns on both sides of the line with $d_1 = 4$ mils and VSWR = 2.	35
22 Maximum (a) Z_{in} error factors and (b) S21 phase error factors for alumina. Results are for 6×16 mil ² tuning bars with $d_2 = 5$ mils, substrate thickness=10 mils, and VSWR = 2. Frequency range: 8-24 GHz.	37
23 Maximum (a) Z_{in} error factors and (b) S21 phase error factors for alumina. Results are for 6×16 mil ² tuning bars with $d_2 = 5$ mils, substrate thickness = 10 mils, and VSWR = 2. Frequency range: 24-40 GHz.	37
24 Maximum (a) Z_{in} error factors and (b) S21 phase error factors for Ferro A6M. Results are for 6×16 mil ² tuning bars with $d_2 = 5$ mils, substrate thickness = 7.4 mils, and VSWR = 2. Frequency range: 8-24 GHz.	38

FIGURE	Page	
25	Maximum (a) Z_{in} error factors and (b) S21 phase error factors for Ferro A6M. Results are for 6×16 mil ² tuning bars with $d_2 = 5$ mils, substrate thickness = 7.4 mils, and VSWR = 2. Frequency range: 24-40 GHz.	38
26	Typical 10×10 mil ² TFN RTCC.	39
27	Simulated (a) Z_{in} , (b) S21 magnitude, and (c) S21 phase error factors for alumina. Results are for 10×10 mil ² tuning bars arranged in five columns on both sides of the line with $d_1 = 5$ mils, $d_2 = 10$ mils, and VSWR=1.....	41
28	Simulated maximum (a) Z_{in} , (b) S21 magnitude, and (c) S21 phase error factors for alumina. Results are for 10×10 mil ² tuning bars arranged as one row-by-five columns on both sides of the line with $d_1 = 4$ mils and VSWR = 2.	43
29	Maximum (a) Z_{in} error factors and (b) S21 phase error factors for alumina. Results are for 10×10 mil ² tuning bars with $d_2 = 5$ mils, substrate thickness = 10 mils, and VSWR = 2. Frequency range: 8-24 GHz.	45
30	Maximum (a) Z_{in} error factors and (b) S21 phase error factors for alumina. Results are for 10×10 mil ² tuning bars with $d_2 = 5$ mils, substrate thickness = 10 mils, and VSWR = 2. Frequency range: 24-40 GHz.	45
31	Maximum (a) Z_{in} error factors and (b) S21 phase error factors for Ferro A6M. Results are for 10×10 mil ² tuning bars with $d_2 = 5$ mils, substrate thickness = 7.4 mils, and VSWR = 2. Frequency range: 8-24 GHz.	46
32	Maximum (a) Z_{in} error factors and (b) S21 phase error factors for Ferro A6M. Results are for 10×10 mil ² tuning bars with $d_2 = 5$ mils, substrate thickness = 7.4 mils, and VSWR = 2. Frequency range: 24-40 GHz.	46
33	Layout of measured stub resonator (a) with and (b) without tuning bars. $\epsilon_r = 10.5$, $h = 10$ mils.	49
34	Simulated vs. measured S21 curve of a stub resonator for (a) $h = 10$ mils and (b) $h = 25$ mils. $\epsilon_r = 10.5$	50

FIGURE	Page
35 (a) Measured and (b) simulated resonant circuit with and without the tuning bars. $\epsilon_r = 10.5$, $h = 10$ mils.	51
36 (a) Measured and (b) simulated resonant circuit with and without the tuning bars. $\epsilon_r = 10.5$, $h = 25$ mils.	52
37 An NRI medium refracts an incident plane wave at a negative angle with the surface normal.	61
38 One-dimensional composite NRI TL unit cell.	62
39 Dispersion diagram for the NRI TL of Fig. 38 for the unmatched case $\sqrt{L_N/C_N} \neq Z_0$	66
40 Dispersion diagram for the NRI TL of Fig. 38 for the matched case $\sqrt{L_N/C_N} = Z_0$	66
41 Schematic diagram of the zeroth order NIR gap coupled line resonator...	69
42 Photograph of the proposed line resonator circuit compared to a conventional gap coupled resonator at 1.2 GHz.	70
43 Measured results for proposed and conventional gap coupled line resonators.	70
44 (a) Layout and (b) condition for resonance for ring resonator using an NRI TL section.	71
45 (a) Layout and (b) condition for resonance for ring resonator with an inner diameter of zero using an NRI TL section.	72
46 Measured results for proposed ring resonators.	74

CHAPTER I

INTRODUCTION

This thesis covers two separate research topics both related to the design of compact microwave circuits. The first topic involves determining the distance that post production tuning bars need to be from the microstrip thru line to cause a negligible effect when they are not used. Various methods exist that could be applied to this problem including analytical methods, even-odd mode analysis, or numerical methods. In this thesis, a commercially available, numerical electromagnetic simulator is used due to its accuracy, practicality, and adaptability to various tuning bar geometries. The second topic is on the design of compact resonators using the transmission line approach of negative refractive index metamaterials.

Chapter II covers the tuning bar research. The chapter starts with an introduction giving the statement of work, objectives, and research methods and approach. Next, various typical GaAs MMIC tuning bar configurations are analyzed followed by the thin film network configurations. The majority of the results are presented in distance-from-the-line plots for various defined error factors. Next, measurement results are presented which experimentally validate the electromagnetic simulations used. Based on the findings, the chapter concludes with recommended tuning bar offset distances. This data can be used to design compact tuning bar configurations with minimum parasitic coupling, thus saving valuable chip space without sacrificing functionality.

Chapter III is on the design of compact resonators using the transmission line approach of negative refractive index metamaterials. A survey of the major developments and fundamental concepts related to negative refractive index technology is given. Next, the transmission line approach is reviewed. This approach bridges general negative refractive index concepts to planar microwave circuits. Following is the

This thesis follows the style and format of the *IEEE Transactions on Microwave Theory and Techniques*.

design and measurement of the compact gap-coupled resonators. Both line and ring resonators are introduced and compared to their conventional counterparts to demonstrate both compactness and harmonic suppression. The new resonators are expected to find many applications in the design of new microstrip filters and oscillators.

CHAPTER II

POST PRODUCTION TUNING BAR ERROR IN MICROWAVE CIRCUITS

A. Introduction

Tuning bars are often used in microwave designs to allow a microstrip line to be lengthened or to allow the impedance of a microstrip line to be tuned in postproduction. In monolithic microwave integrated circuit (MMIC) design, the tuning bars can look like horseshoes or rectangular bars. In module design, the bars are typically rectangular metal patterns with various degrees of spacing. Ideally, unused tuning bars should have a negligible effect on the circuit's overall performance. To achieve a negligible effect, conventional wisdom suggests placing the tuning bars 1.0 to 1.5 substrate heights away from the main line.

1. Statement of Work

Raytheon Company sponsored the research conducted for this thesis. The statement of work applicable to this thesis is:

Electromagnetic simulations and fabricated test structures on various substrates should be used to show how far the tuning bars need to be from the microstrip line to cause a negligible effect when they are not used.

2. Objectives

The objective of the work presented in this chapter is to characterize the tuning bar error, defined as the deviation from the unaffected case in the transmission of a signal along the perturbed line, associated with different unused microstrip tuning bar geometries for a variety of practical distances and dimensions. The error is primarily

determined through electromagnetic simulations, and the accuracy of these simulations is verified by experimental measurements. The effect of load mismatch on the tuning bar error is also investigated.

Although a hard criterion for “negligible effect” is not given, one goal of this thesis is to recommend possible tuning bar offset distances based on the error analysis findings. Minimizing this offset distance saves valuable space on a circuit board and therefore leads to more compact designs and direct financial savings.

3. Simulation and CAD Software

In this thesis, the tuning bar configurations are simulated with Sonnet v. 8.52 [1], a full-wave electromagnetic simulator using a modified Method of Moments analysis. Sonnet was chosen above other simulators partly based on a previous student’s recommendation and experiences with modeling electrically small passive elements on 100 um GaAs MMICs [2]. In addition, Sonnet was compared with IE3D [3] through numerous simulations, and Sonnet was found to be more stable and accurate over a wide range of meshing and port schemes. Agilent’s Advanced Design System (ADS) [4] is also used in this chapter for performing optimization procedures.

4. Research Methods and Approach

In this chapter both GaAs MMIC and alumina/Ferro A6M TFN tuning bar configurations with parameters specified by Raytheon are analyzed. The tuning bar error factors, which include S21 magnitude error, S21 phase error, and Z_{in} error, are determined through the following systematic approach. First, Sonnet is used to simulate the tuning bar configuration in a matched system both with and without the tuning bars. The resulting S-parameters are then imported into ADS where ADS’s optimization capabilities are employed to find the maximum tuning bar errors for a specified VSWR and frequency. In addition, a resonant frequency error analysis is performed which involves simulating a stub resonator with and without the tuning bar configuration and observing the change in resonant frequency. Finally, the accuracy of Sonnet and the

simulation settings used in this chapter is demonstrated by comparing both measurement and simulation of a quarter-wave open stub resonator with and without tuning bars.

5. Summary

This chapter details the study of the parasitic effects and error associated with different unused microstrip tuning bar geometries for a variety of practical distances and dimensions. Defined as the deviation of a signal along the perturbed line compared to a line with no tuning bars, the error is primarily determined through electromagnetic simulations using Sonnet, and the accuracy of these simulations is verified by experimental measurements. The aim of this chapter is to facilitate the design of compact tuning bar configurations with minimum parasitic effects which will lead to a savings of chip space and consequently money.

B. GaAs MMIC Tuning Bar Configuration

A study on the error associated with unused tuning bars on 100 μm GaAs substrate is performed. The common GaAs MMIC tuning bar configuration consists of an airbridge (AB) with a single tuning bar offset from the main thru-line. When tuning the line (i.e. extending the length of the line), one simply breaks the AB and bonds the tuning bar to the main line. Foundry rules dictate a maximum AB length of 100 μm . If longer tuning stubs are required, a U shaped tuning bar is used instead of a rectangular bar.

Fig. 1 shows the layout of the rectangular tuning bar configuration. The GaAs dielectric constant; $\epsilon_r = 12.9$, substrate thickness = 100 μm , substrate loss tangent; $\tan \delta = 0.0004$, gold metallization thickness = 5 μm , air gap thickness = 2 μm , and tuning bar overlap = 20 μm . The line impedances of interest are 25 Ω , 50 Ω , and 100 Ω . Using both TX-Line [5] and IE-3D Line Gauge [6], the corresponding line widths at 10 GHz are approximately 256 μm , 70 μm , and 5 μm , respectively. In this thesis the AB is ignored for $L > 100 \mu\text{m}$, because AB's longer than 100 μm are not currently used in

practice. This is justified since it was found through simulation that the parasitic effects of the tuning bar are practically independent of the AB, which is reasonable because the gap is very thin (the metal thickness is over twice the thickness of the air gap.)

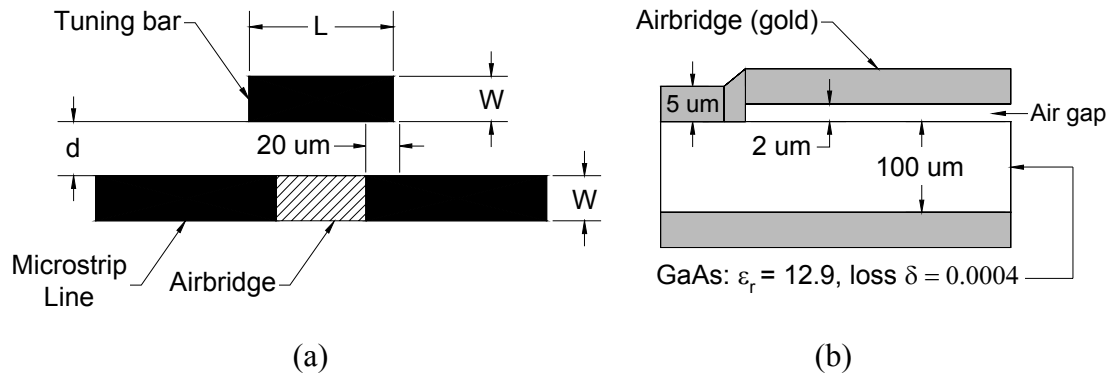


Fig. 1 (a) Top and (b) side view of rectangular GaAs MMIC tuning bar configuration.

When simulating the tuning bar configuration, the microstrip thru line is extended out 68 μm beyond the tuning bar in both directions to account for any fringing fields as shown in Fig. 2 (a). A closed form expression giving the edge extension accounting for these fringing fields is given in [7]. To extract the error associated with the tuning bar, two identical microstrip lines with and without the tuning bar are compared. Fig. 2 (b) shows the reference thru line used for comparison. Note that if the AB is included in the analysis, both the tuning bar configuration and reference thru line contain the AB.

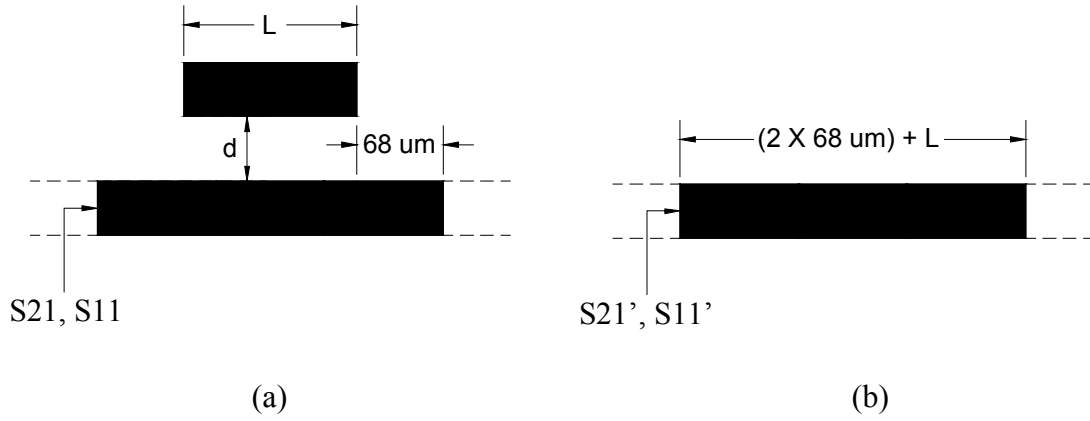


Fig. 2 Simulated GaAs MMIC (a) rectangular tuning bar configuration and (b) reference thru line.

This thesis uses the following S21 error factors when calculating the error or parasitic effect caused by the tuning bars.

$$\text{S21 Magnitude Error (\%)} = 100 \cdot \frac{|S21| - |S21'|}{|S21'|}, \quad |S21'| \neq 0 \quad (1)$$

$$\text{S21 Phase Error (Degrees)} = \text{Phase}(S21) - \text{Phase}(S21') \quad (2)$$

where S21 and S21' represent complex valued S21 parameters for the microstrip line with and without the tuning chips respectively. Also, the following Z_{in} error factors are used.

$$\text{Re}(Z_{in}) \text{ Error } (\Omega) = \text{Re}\{Z_{in} - Z_{in}'\} \quad (3)$$

$$\text{Im}(Z_{in}) \text{ Error } (\Omega) = \text{Im}\{Z_{in} - Z_{in}'\} \quad (4)$$

$$Z_{in} \text{ Error (\%)} = 100 \cdot \frac{|Z_{in} - Z_{in}'|}{|Z_{in}'|}, \quad |Z_{in}'| \neq 0 \quad (5)$$

where Z_{in} and Z_{in}' represent the complex input impedance values for the microstrip line with and without the tuning bars, respectively.

1. Matched Load

For a matched load, Z_{in} and S21 (both primed and unprimed) are simulated in a system with the same termination impedances as that of the microstrip thru line. For example, when measuring Z_{in} and S21 for a 25 Ω line, the feed lines and terminations (both port 1 and port 2) are 25 Ω .

An error analysis is performed on the following three important cases:

1. Typical case: $L = 100$ μm , $d = 100$ μm , AB included. This case incorporates standard dimensions used in practice. That is, the tuning bar is placed one substrate height away from the line ($d = 100$ μm) and the length of the tuning bar is typical for circuits on GaAs. For this case, the AB is included in the simulation.
2. Worst case specified by Raytheon: $L = 200$ μm , $d = 50$ μm , AB not included. This case includes the minimum tuning bar offset distance ($d = 50$ μm) and maximum length ($L = 200$ μm) specified by Raytheon for this thesis. Raytheon expected this case to cause a large error. The AB is not included in the simulation.
3. Absolute worst case: $L = 200$ μm , $d = 5$ μm , AB not included. This case includes the minimum gap spacing that can currently be fabricated on GaAs ($d = 5$ μm) for the maximum specified length. The AB is not included in the simulation.

Table I gives the simulated error results for these three cases. For convenience, the maximum error in each category is shaded grey.

TABLE I
SIMULATED GAAS TUNING BAR ERROR RESULTS FOR THREE IMPORTANT CASES. ERRORS
ARE FOR MATCHED LOAD (VSWR=1).

Typical case: $L = 100 \text{ um}$, $d = 100 \text{ um}$, AB Included

	Frequency (GHz)	Re{ Z_{in} Error} (Ω)	Im{ Z_{in} Error} (Ω)	Z_{in} Error (%)	S21 Magnitude Error (%)	S21 Phase Error (Degrees)
25 Ohm ($W = 256 \text{ um}$)	10	-0.0013	-0.0114	0.0457	-0.0006	-0.0014
	35	-0.0152	-0.0286	0.1286	-0.0010	0.0006
50 Ohm ($W = 70 \text{ um}$)	10	-0.0011	-0.0144	0.0288	-0.0007	0.0005
	35	-0.0205	-0.0440	0.0951	-0.0012	0.0030
100 Ohm ($W = 5 \text{ um}$)	10	0.0001	-0.0003	0.0003	0.0000	0.0000
	35	0.0000	-0.0009	0.0009	-0.0001	-0.0001

Worst case specified by Raytheon: $L = 200 \text{ um}$, $d = 50 \text{ um}$, AB not Included

	Frequency (GHz)	Re{ Z_{in} Error} (Ω)	Im{ Z_{in} Error} (Ω)	Z_{in} Error (%)	S21 Magnitude Error (%)	S21 Phase Error (Degrees)
25 Ohm ($W = 256 \text{ um}$)	10	-0.0193	-0.0971	0.3945	-0.0053	-0.0144
	35	-0.2112	-0.2146	1.2200	-0.0197	-0.0333
50 Ohm ($W = 70 \text{ um}$)	10	-0.0208	-0.1313	0.2643	-0.0057	-0.0036
	35	-0.2879	-0.3418	0.8891	-0.0155	-0.0087
100 Ohm ($W = 5 \text{ um}$)	10	0.0001	-0.0034	0.0033	-0.0003	-0.0003
	35	-0.0046	-0.0082	0.0087	-0.0005	-0.0018

Absolute worst case: $L = 200 \text{ um}$, $d = 5 \text{ um}$, AB not Included

	Frequency (GHz)	Re{ Z_{in} Error} (Ω)	Im{ Z_{in} Error} (Ω)	Z_{in} Error (%)	S21 Magnitude Error (%)	S21 Phase Error (Degrees)
25 Ohm ($W = 256 \text{ um}$)	10	-0.1061	-0.5161	2.0994	-0.0373	-0.2351
	35	-1.2564	-1.1912	6.9942	-0.1773	-0.7862
50 Ohm ($W = 70 \text{ um}$)	10	-0.1379	-0.8511	1.7138	-0.0447	-0.1112
	35	-1.9728	-2.2362	5.9331	-0.1588	-0.3566
100 Ohm ($W = 5 \text{ um}$)	10	-0.0007	-0.1155	0.1121	-0.0082	-0.0146
	35	-0.2257	-0.4168	0.4413	-0.0289	-0.0382

For a matched load, the simulated results shown in Table I validate the conventional wisdom that suggests unused tuning bars placed one substrate height away from the thru line causes negligible effect. Moreover, if the criterion for “negligible effect” is chosen so that the error factors, Z_{in} and S21 magnitude error, are less than ~1% and the S21 phase error is less than 1 degree, then the tuning bars can be placed at half a substrate height from the line with acceptable error. For case 3 (the absolute worst case), the error does become unacceptable for lines with characteristic impedances of 25 and

50 Ohms. It should also be noted that the tuning bar configurations are simulated between 8 and 40 GHz, and for a matched load the error factors increase almost linearly with frequency.

2. Mismatched Load

Besides tuning bar offset distance and length, the load mismatch also affects the tuning bar error. After many simulations with different terminating impedances, some observations are made. First, the parasitic effects caused by the tuning bars for the mismatched case are generally higher than the matched case. Second, in some cases the error factors do not simply increase with frequency for a given load, but rather oscillate with frequency. Third, the error factors tend to increase as the load mismatch increases (i.e. the VSWR increases).

To efficiently analyze the errors for the mismatched case, the following technique is performed. First, Sonnet is used to simulate the lines with and without the tuning bar for different tuning bar lengths (L) and offset distances (d) in a matched system. Then the S-parameters are imported into ADS. Subsequently, using the optimization capabilities of ADS, the maximum errors for a given frequency and VSWR are extracted. Fig. 3 shows a screenshot of an optimization simulation performed in ADS for the Z_{in} error factor. Port 1 is kept matched to the line (50Ω for the case shown in Fig. 3) and the terminating impedance at port 2 is changed. Using the procedure described above, it is found that the maximum error factors do increase linearly with frequency (as opposed to varying with frequency for a single terminating impedance.) Note that when ADS simulates for a complex load, it outputs the generalized power scattering parameters.

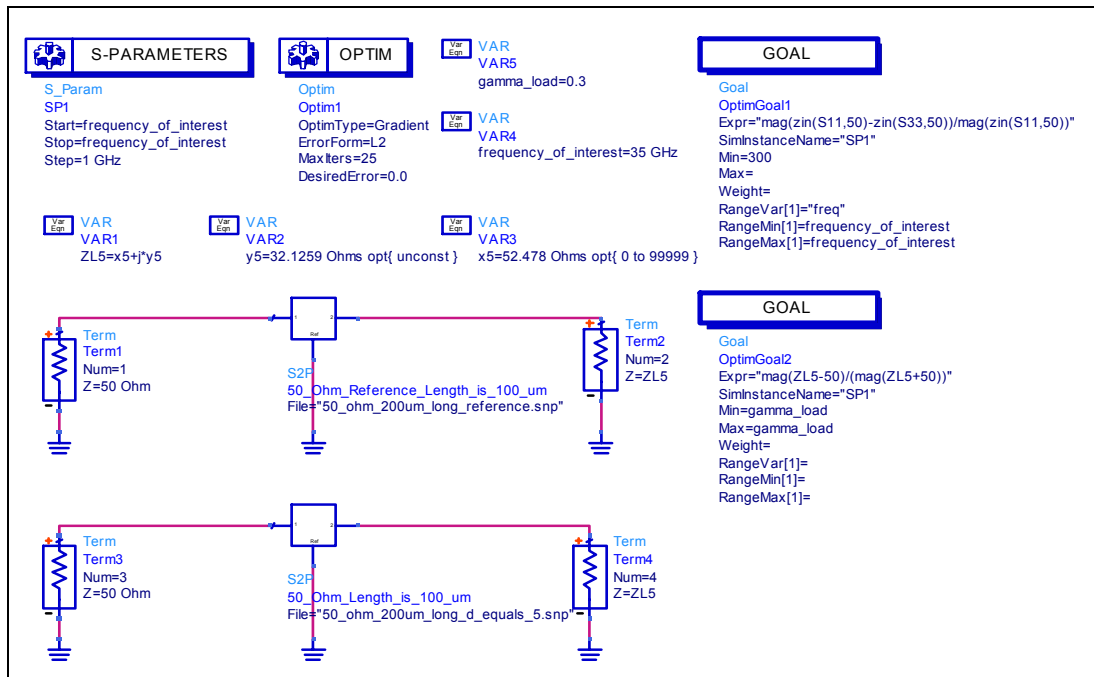
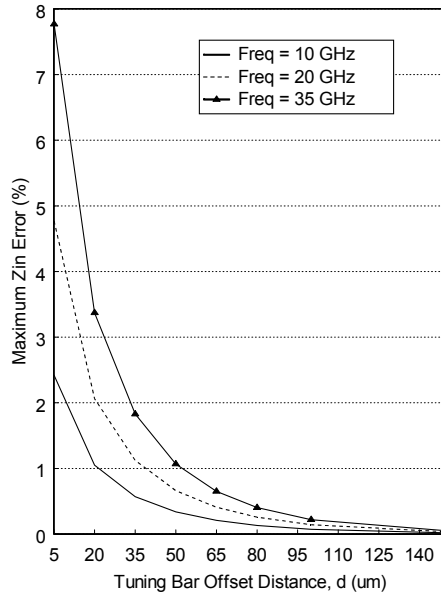


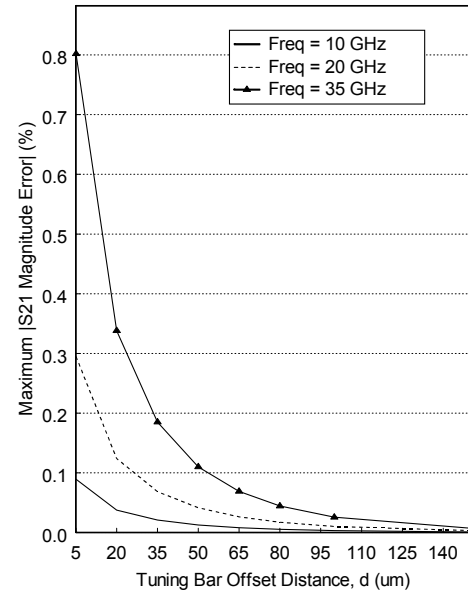
Fig. 3 ADS optimization screenshot

The results of the error maximization procedure for the $Z_0 = 50 \Omega$ and 25Ω cases are shown in Figs. 4 and 5. The results given are for the magnitude of the reflection coefficient $|\Gamma_0| = 1/3$ (VSWR = 2) and $L = 200 \mu\text{m}$ (maximum tuning bar length analyzed in this thesis). Figs. 4 and 5 demonstrate that the error is only significant at very small tuning bar offset distances and that the error exponentially decreases with tuning bar offset distance. The results also show an apparent discrepancy between the Z_{in} and S_{21} magnitude error factors. For instance, in Fig. 4 the Z_{in} error is 8 % while the S_{21} magnitude error is only 0.8 %. This apparent discrepancy is simply because the power absorbed by the load relative to the input power (which is quantified by the magnitude of S_{21} squared), stays almost constant regardless of small changes to the overall input impedance. For example, suppose the input impedance changes from $Z_{in} = 50 \Omega$ to $Z_{in} = 54 \Omega$. While this corresponds to an 8% difference in input impedance, the magnitude of S_{21} for the two cases is calculated to differ by only 0.074% (assuming a lossless and reciprocal network in a 50Ω system).

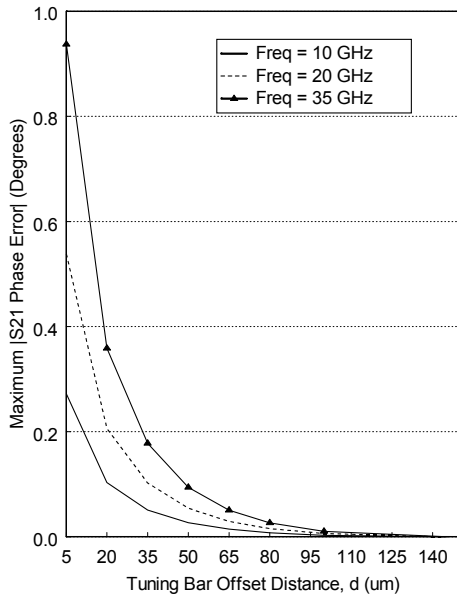
$$Z_0 = 50 \Omega$$



(a)



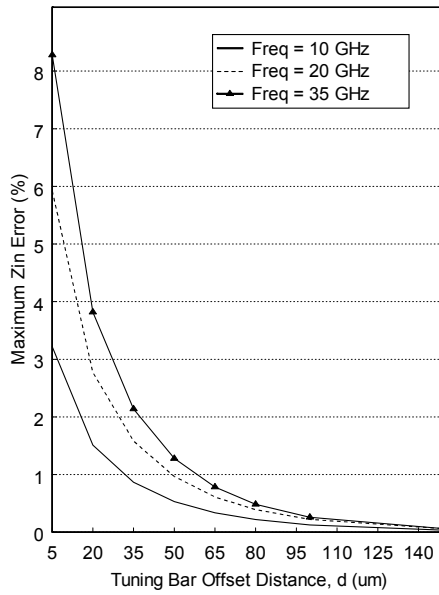
(b)



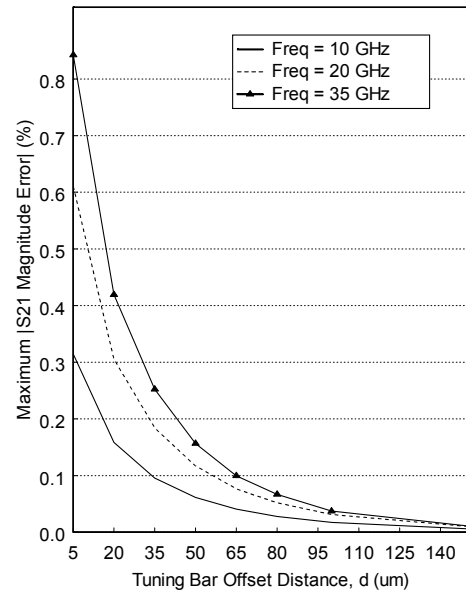
(c)

Fig. 4 Maximum (a) Z_{in} , (b) $|S_{21}$ magnitude|, and (c) $|S_{21}$ phase| error factors. $Z_0 = 50 \Omega$, $L = 200 \mu\text{m}$, substrate thickness = $100 \mu\text{m}$, and VSWR = 2.

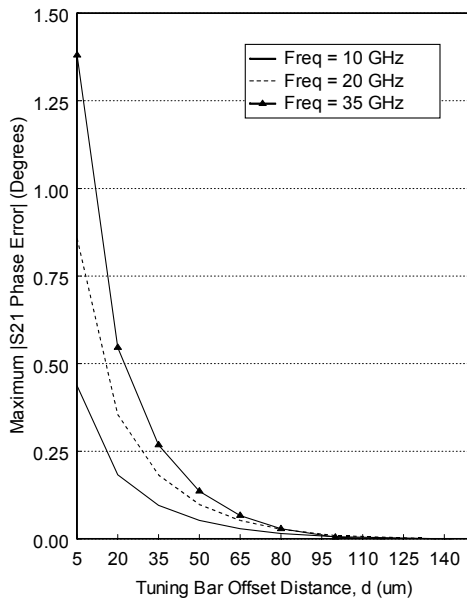
$$Z_0 = 25 \Omega$$



(a)



(b)



(c)

Fig. 5 Maximum (a) Z_{in} , (b) $|S_{21}$ magnitude, and (c) $|S_{21}$ phase error factors. $Z_0 = 25 \Omega$, $L = 200 \mu\text{m}$, substrate thickness = $100 \mu\text{m}$, and VSWR = 2.

For comparison, the maximum Z_{in} error factors for $L = 100 \text{ um}$ and $L = 150 \text{ um}$ are given in Figs. 6 and 7. Overall, it is seen that as the width of the line increases (which corresponds to a decreasing Z_0) the error factors also slightly increase. Also, as one would expect, the error increases as L increases. For $Z_0 = 100 \text{ }\Omega$, the error factors are negligible (Z_{in} error $< 0.1\%$, S_{21} phase error < 0.08 degrees) and are not shown.

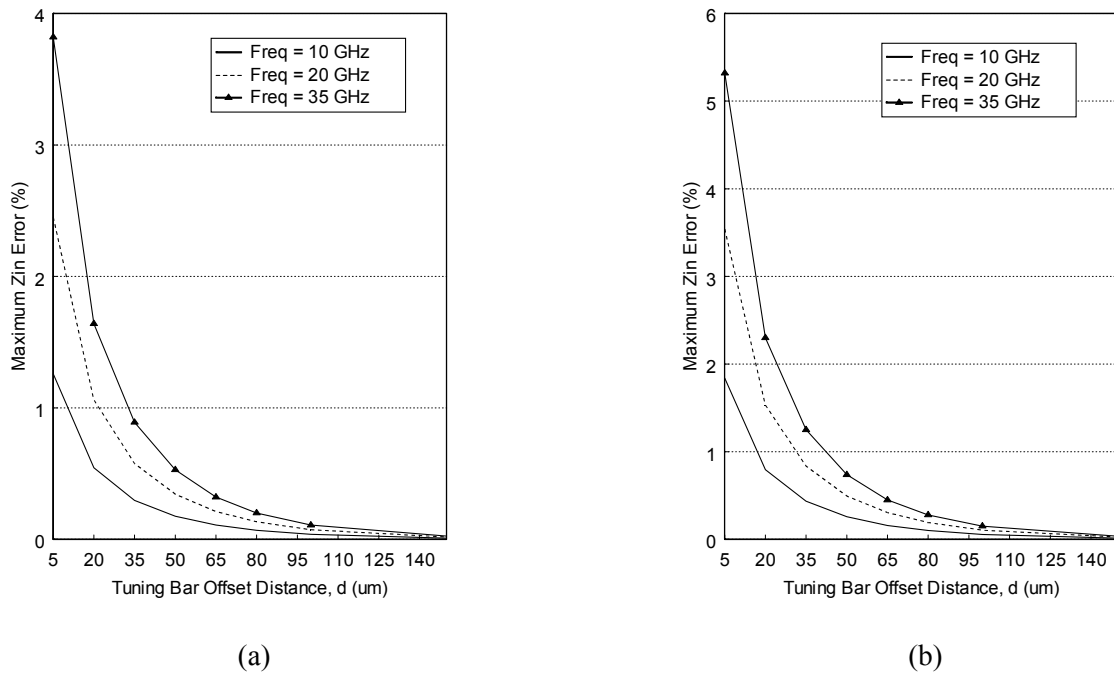


Fig. 6 Maximum Z_{in} error factors for (a) $L = 100 \text{ um}$ and (b) $L = 150 \text{ um}$. Substrate thickness = 100 um , $Z_0 = 50 \text{ }\Omega$, and $VSWR = 2$.

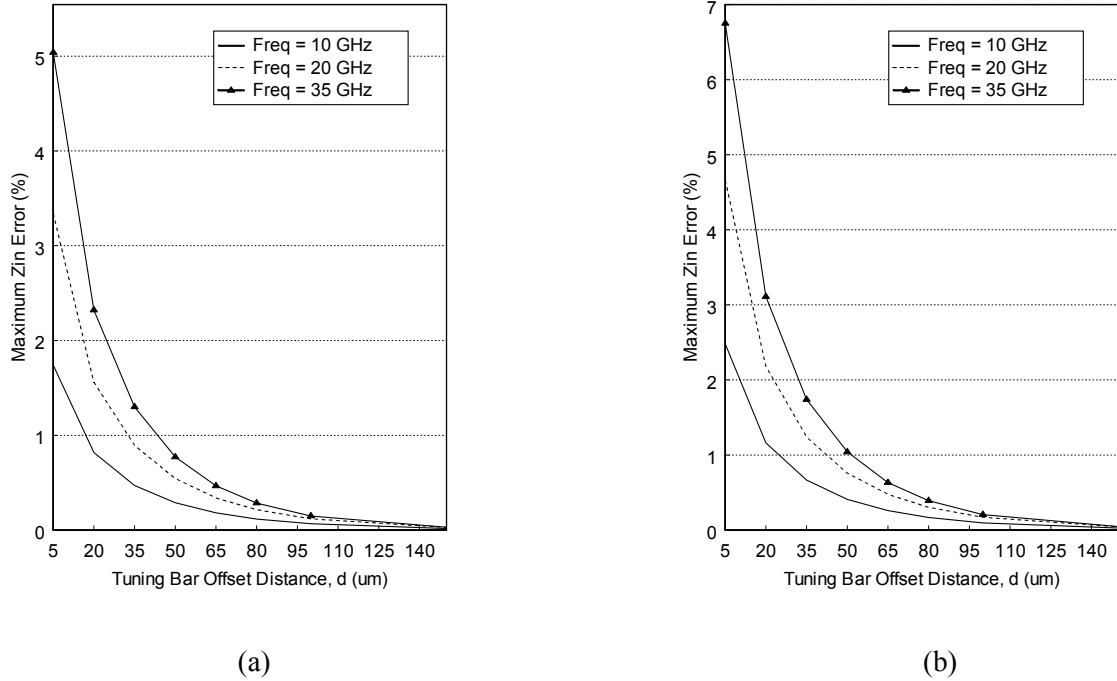


Fig. 7 Maximum Z_{in} error factor for (a) $L = 100$ um and (b) $L = 150$ um. Substrate thickness = 100 um, $Z_0 = 25 \Omega$, and VSWR = 2.

3. Resonant Frequency Error Analysis

Another method of analyzing the parasitic effects of the tuning bar is to simulate a resonant circuit with and without the tuning bar and observe the change in resonant frequency. The resonant frequency error is herein defined as the resonant frequency difference between a quarter-wave stub resonant circuit with and without a tuning bar. Fig. 8 shows the simulated quarter-wave stub resonant circuits with centered offset rectangular tuning bars. In Fig. 8 (a) the circuit is designed to resonant at around 10 GHz and in Fig. 8 (b) the circuit resonates at 35 GHz. The AB is not included in this analysis because its effects are particularly small.

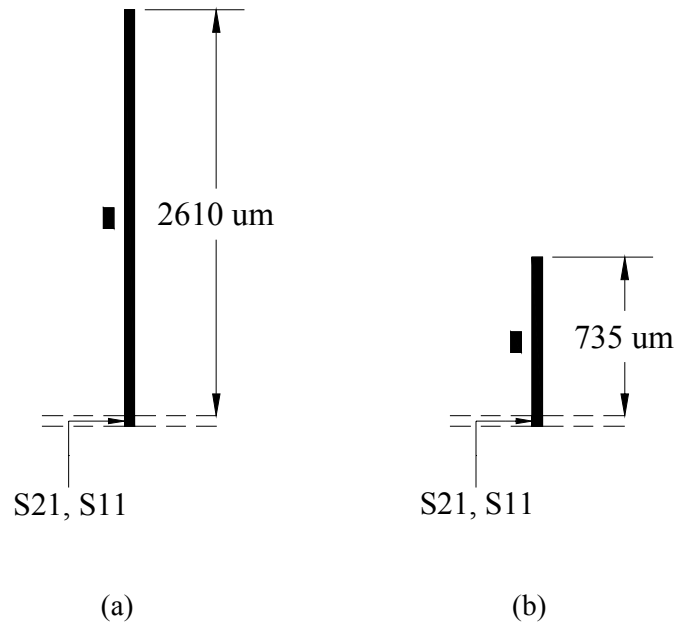


Fig. 8 GaAs MMIC quarter wave stub resonant circuit at (a) 10 GHz and (b) 35 GHz with rectangular tuning bar.

Table II gives the simulated resonant frequency errors for the three cases: typical, worst case specified by Raytheon, and absolute worst case. It is seen that the errors for both the typical and worst case specified by Raytheon are less than 0.04% and negligible. For the absolute worst case, the errors become slightly more significant for the 25 Ω and 50 Ω lines, with errors ranging between around 0.1% and 0.36%.

TABLE II
SIMULATED GAAS QUARTER WAVE STUB RESONANT FREQUENCY ERROR RESULTS FOR
THREE IMPORTANT CASES.

Typical case: $L = 100 \text{ um}$, $d = 100 \text{ um}$, AB Not Included

	Approx. Resonant Frequency (GHz)	Resonant Frequency Error (MHz)	Resonant Frequency Error (%)
25 Ohm ($W = 256 \text{ um}$)	10	Error < 1	Error < 0.01
	35	3	Error < 0.01
50 Ohm ($W = 70 \text{ um}$)	10	Error < 1	Error < 0.01
	35	2	Error < 0.01
100 Ohm ($W = 5 \text{ um}$)	10	Error < 1	Error < 0.01
	35	Error < 1	Error < 0.01

Worst case specified by Raytheon: $L = 200 \text{ um}$, $d = 50 \text{ um}$, AB not Included

	Approx. Resonant Frequency (GHz)	Resonant Frequency Error (MHz)	Resonant Frequency Error (%)
25 Ohm ($W = 256 \text{ um}$)	10	Error < 1	Error < 0.01
	35	14	0.04
50 Ohm ($W = 70 \text{ um}$)	10	Error < 1	Error < 0.01
	35	12	0.034
100 Ohm ($W = 5 \text{ um}$)	10	Error < 1	Error < 0.01
	35	Error < 1	Error < 0.01

Absolute worst case: $L = 200 \text{ um}$, $d = 5 \text{ um}$, AB not Included

	Approx. Resonant Frequency (GHz)	Resonant Frequency Error (MHz)	Resonant Frequency Error (%)
25 Ohm ($W = 256 \text{ um}$)	10	-16	-0.16
	35	-129	-0.369
50 Ohm ($W = 70 \text{ um}$)	10	-9	-0.09
	35	-37	-0.11
100 Ohm ($W = 5 \text{ um}$)	10	-2	-0.02
	35	-22	-0.062

4. Equivalent Circuit

In practice, one typically does not take the time to model the actual tuning bar configuration. Instead, guided by conventional wisdom, the designer simply places the

tuning bar at a certain offset distance away from the thru line (usually a distance of about 1.0 to 1.5 substrate heights), and assumes the tuning bar's effects are negligible. One goal of this thesis is to test the validity of this convention and recommend a more optimum offset distance depending on the configuration. Therefore, modeling the tuning bar configurations is not the primary focus here. That being said, an equivalent circuit or model does help gain more insight into the effects of the tuning bar.

The rectangular tuning bar configuration on GaAs substrate essentially involves a microstrip thru line parallel coupled to another microstrip line section that is open circuited at both ends. This parallel coupled transmission line circuit is shown in Fig. 9 (a). Since both the thru line and the tuning bar have the same width, the effects of the tuning bar can be analyzed (at least approximately) through the use of even-odd mode analysis and has the equivalent circuit shown in Fig. 9 (b) [8]. The even and odd mode characteristic impedances of the coupled line system are denoted Z_{0e} and Z_{0o} , respectively. It is seen that the equivalent circuit is simply a transmission line with the same length as the original and with a new characteristic impedance $Z_{0,eq} = (Z_{0e} + Z_{0o})/2$. Using filter terminology, this is an all pass network. It should be noted that the equivalent circuit is valid for TEM operation only, and it also ignores edge effects. Therefore, the equivalent circuit only approximately models the coupled microstrip tuning bar configuration (which supports quasi-TEM modes), and it therefore may not accurately predict the minute tuning bar errors which are reported in this thesis.

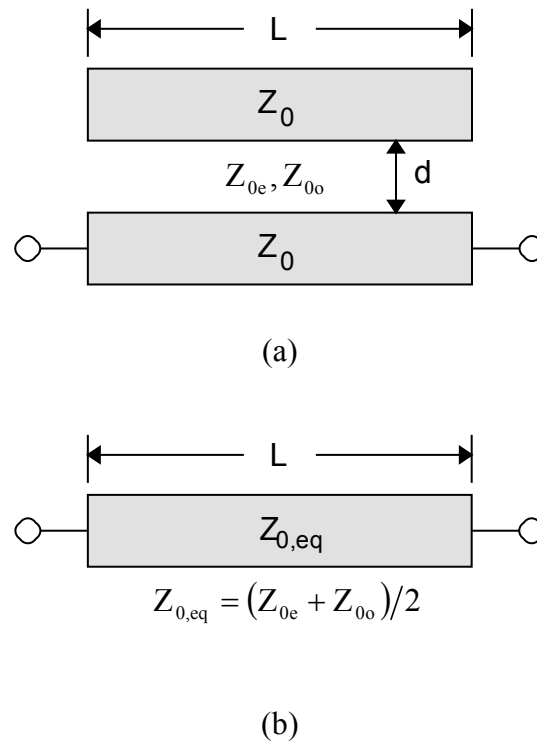


Fig. 9 Tuning bar configuration. (a) Coupled line section representation and (b) equivalent circuit.

From the equivalent circuit in Fig. 9 (b), it is apparent why the tuning bar error increases with frequency. First, the electrical length of the equivalent circuit transmission line segment increases with frequency. As the electrical length increases, the effect on circuit performance due to the difference between the perturbed transmission line's characteristic impedance $Z_{0,eq}$ and the unperturbed transmission line's characteristic impedance Z_0 becomes more pronounced.

Based on the tuning bar configuration's equivalent circuit shown in Fig. 9, there are two reasons why the parasitic errors are small. The first reason is that the tuning bars used are electrically short. For example, the electrical length of the 200 μm bars on GaAs is only about 7 degrees at 10 GHz. The second reason is that $Z_{0,eq}$ and Z_0 are very similar. As an example, consider the tuning bar configuration with an offset distance $d =$

50 μm (half a substrate height), operating frequency at 10 GHz, with a line characteristic impedance of $Z_0 = 25 \Omega$. Using Txline software, the calculated characteristic impedance of the perturbed line $Z_{0,\text{eq}} = 23.4 \Omega$. Therefore, it is seen that $Z_{0,\text{eq}}$ only deviates slightly from Z_0 (about 6%). The corresponding VSWR and $|S_{11}|$ (in a 50 Ohm system) are 1.016 and -41.8 dB. Therefore, the equivalent circuit model also predicts very little error (or mismatch) attributed to the adjacent tuning bar.

Another interesting observation is that the parasitic effects of the tuning bar are not necessarily dependent on the strength of the electromagnetic coupling as quantified by the coupling coefficient $C = (Z_{0e} - Z_{0o}) / (Z_{0e} + Z_{0o})$. This coupling coefficient dictates how much power can be coupled from one line to another for coupled line directional couplers [8]. From the tuning bar configuration's equivalent circuit, one can see that the parasitic effects increase as the value of $Z_{0,\text{eq}}$ strays from the value of Z_0 . Because $Z_{0,\text{eq}} = (Z_{0e} + Z_{0o}) / 2$, the difference between Z_0 and $Z_{0,\text{eq}}$ (which results in tuning bar error) is not necessarily dependent on the difference between Z_{0e} and Z_{0o} . That is to say, the magnitude of the tuning bar error is not necessarily dependent on the coupling coefficient.

5. *U-Shaped Tuning Bars*

In practice, U-shaped (or horseshoe-shaped) tuning bars are used instead of rectangular tuning bars if tuning bar lengths greater than 100 μm are needed. Fig. 10 shows the layout of the GaAs MMIC U-shaped tuning bar configuration analyzed in this thesis. While Fig. 10 includes an AB, the AB is not actually simulated due to enormous computation times. The simple formula, $L_{\text{path}} = \pi \cdot (r + W/2)$ gives the mean (average) path length, L_{path} , of the U-shaped tuning bar with an inner radius, r , and a width, W . The effective length including the end effects is slightly larger. In this thesis $r = 50 \mu\text{m}$. Therefore, $L_{\text{path}} = 165 \mu\text{m}$, $267 \mu\text{m}$, and $560 \mu\text{m}$ for the 100 Ω , 50 Ω , and 25 Ω cases, respectively. Compared to the rectangular tuning bar, the length of the U-shaped tuning bar is larger and the end effects make the effective gap size smaller.

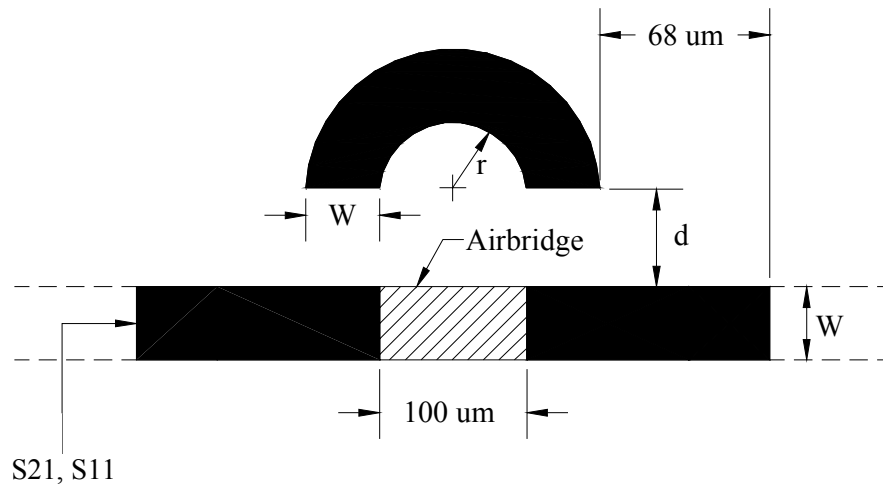


Fig. 10 GaAs MMIC U-shaped tuning bar configuration.

The error maximization procedure for a mismatched load is performed on the U-shaped tuning bar configuration. The results are shown in Figs. 11 and 12 for $Z_0 = 50\ \Omega$ and $Z_0 = 25\ \Omega$ with $|\Gamma_0| = 1/3$ (VSWR = 2). Compared to the previous straight bar cases, the errors for the U-shaped bar are worse for $Z_0 = 25\ \Omega$, but almost the same for $Z_0 = 50\ \Omega$. This is due to the comparatively large L_{path} for the $Z_0 = 25\ \Omega$ case. For $Z_0 = 100\ \Omega$, the error factors are negligible and are not shown.

$$Z_0 = 50 \Omega$$

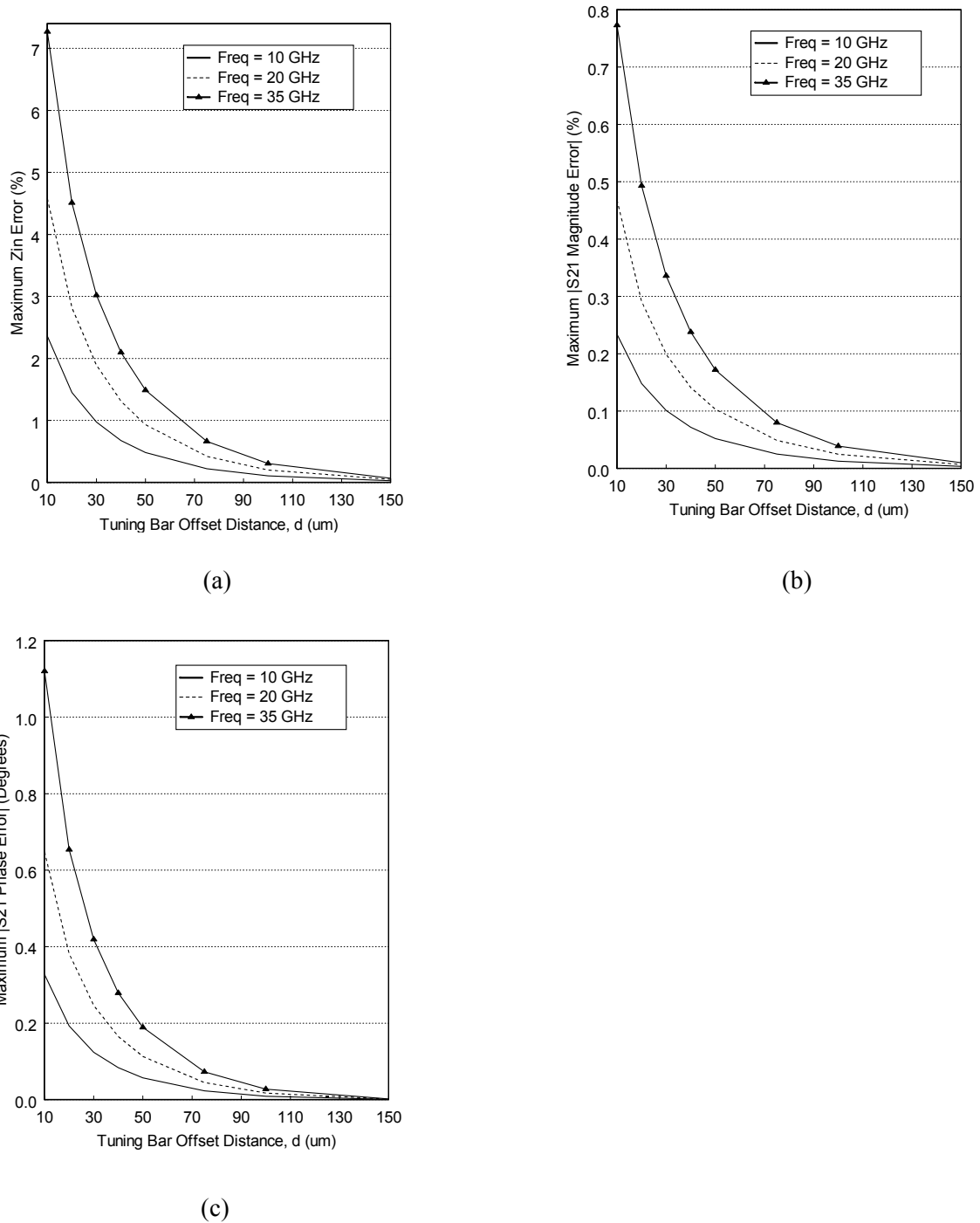
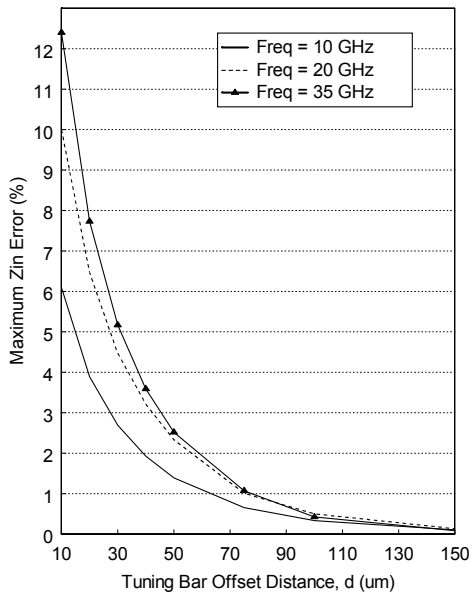
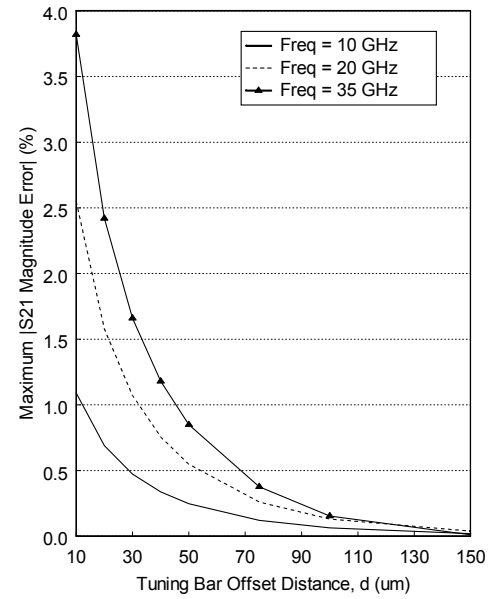


Fig. 11 Maximum (a) Z_{in} , (b) $|S_{21}|$ magnitude, and (c) $|S_{21}|$ phase error factors for U-shaped tuning bar. $Z_0 = 50 \Omega$, substrate thickness = 100 μm , $L_{\text{path}} = 267 \mu\text{m}$, and VSWR = 2.

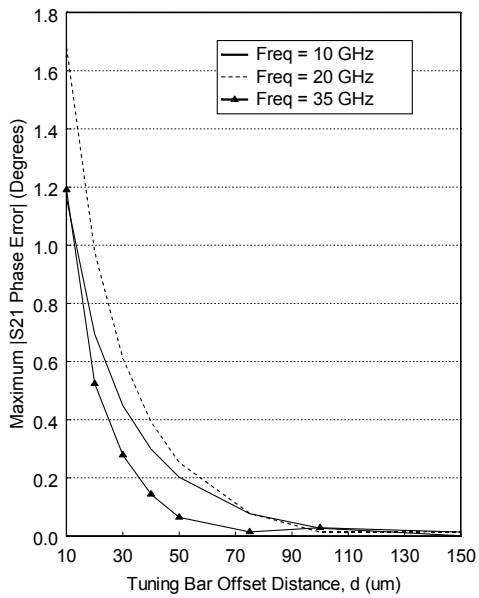
$$Z_0 = 25 \Omega$$



(a)



(b)



(c)

Fig. 12 Maximum (a) Z_{in} , (b) $|S_{21}$ magnitude|, and (c) $|S_{21}$ phase| error factors for U-shaped tuning bar. $Z_0 = 25 \Omega$, substrate thickness = 100 μm , $L_{\text{path}} = 560 \mu\text{m}$, and VSWR = 2.

6. Conclusions

The current practice of placing tuning bars one substrate height away from the main thru line for GaAs MMIC's is quite conservative. Using the results given in this chapter allows the tuning bars to be confidently placed at shorter distances. In general the tuning bar error increases as the load mismatch and, subsequently, the VSWR increases. Finally, the U-shaped tuning bar results in higher error compared to the rectangular shaped bar.

C. Thin Film Network (TFN) Tuning Bar Configurations

A study on the error associated with unused tuning bars on 10 mil (thickness) alumina and 7.4 mil Ferro A6M substrate is performed. The two common TFN tuning bar configurations are the line-lengthening tuning stub and the rectangular tuning chip cluster configurations. Line-lengthening tuning stubs consist of multiple rectangular bars offset at the end of an open microstrip line. When tuning the line (i.e. extending the length of the open line), one simply bonds the tuning bars to the open microstrip line. The rectangular tuning chip cluster configuration includes a number of small rectangular bars flanking the main thru line. When tuning the line (i.e. changing the impedance of the thru line), one bonds the tuning bars to the main thru line.

In this section, the tuning bar error is inspected for two common TFN substrate materials, alumina and Ferro A6M. Nominal parameters for the two substrates used throughout this section are as follows. Alumina dielectric constant; $\epsilon_r = 9.65$, substrate thickness = 10 mils, substrate loss tangent; $\tan \delta = 0.001$, and gold metallization thickness = 0.1 mils. Ferro A6M dielectric constant; $\epsilon_r = 6.1$, substrate thickness = 7.4 mils, substrate loss tangent; $\tan \delta = 0.0012$, and gold metallization thickness = 0.4 mils. The line impedance of interest is 50Ω . Using TX-Line for the specified parameters, the corresponding line widths at 10 GHz for alumina and Ferro A6M are approximately 10 and 11 mils, respectively.

1. Line-Lengthening Tuning Stub Configuration

Fig. 13 shows the layout of the TFN line-lengthening tuning stub configuration. As shown in the figure, the dimensions of the tuning bars are typically $W \times W/2$, where W is the width of the microstrip line. In practice, there can be more than three stubs and the distances between the stubs are not necessarily equal.



Fig. 13 Typical TFN line-lengthening tuning stub geometry.

When simulating, the feed line is de-embedded as shown in Fig. 14. In the figure, two parallel dashed lines represent the de-embedded feed line. The length of the microstrip line is equal to the width of the line. This is chosen arbitrarily and no generality is lost by this de-embedding scheme. The distance between the microstrip line and the first tuning bar is d_1 ; the distance between the first and second tuning bars is d_2 , etc.

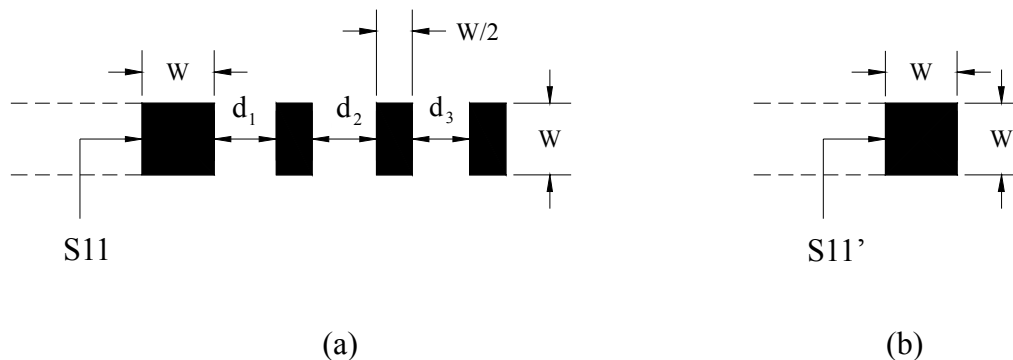


Fig. 14 Simulated TFN (a) line-lengthening tuning stub configuration and (b) reference thru line after de-embedding.

For practical purposes, only the first two tuning bars closest to the line need to be taken into account for error analysis. To illustrate this, the line-lengthening tuning stub configuration is simulated with one, two, four, and eight tuning bars. Fig. 15 shows the simulated Z_{in} error (%). The results shown in the figure are for the worst-case error (i.e. the minimum distance that can be fabricated on these substrates). This corresponds to a distance (d_1, d_2, \dots, d_8) of 1 mil for alumina and 2 mils for Ferro A6M.

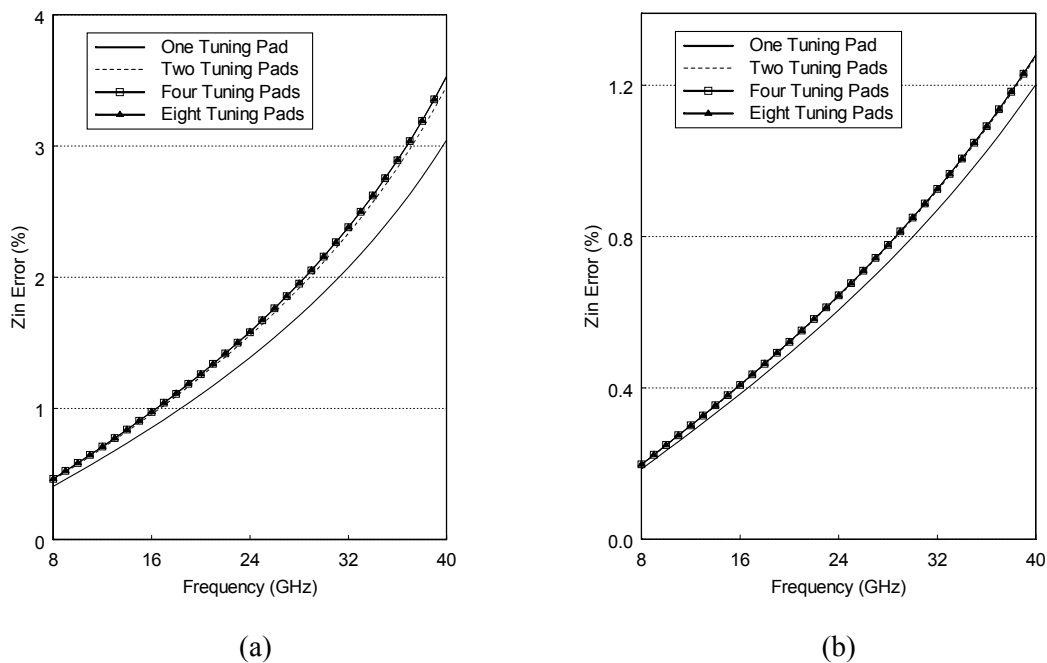


Fig. 15 Simulated worst-case Z_{in} error factors for (a) alumina and (b) Ferro A6M for one, two, four, and eight line-lengthening stubs.

As Fig. 15 shows, the Z_{in} error factor for a line-lengthening tuning stub configuration (even with minimum distances) is dependent solely on the first two tuning bars. In other words, the error from eight tuning bars is the same as the error from only two tuning bars. Furthermore, it is seen that about 90% of the error is due to the first tuning bar, and so the error is much more dependent on d_1 than on d_2 . Because of the

above observations, only the first two tuning bars will be included in the following simulations, and as a simplification, d_2 is taken to equal d_1 ($d_2 = d_1 = d$).

An error analysis for three important tuning bar offset distances, d , is now performed. For alumina, d is varied as 10 mils (substrate height), 5 mils (half the substrate height), and 1 mil (minimum distance). For Ferro A6M, d is varied as 8 mils (\sim substrate height), 4 mils (\sim half the substrate height), and 2 mils (minimum distance). These cases represent the typical, compact (worse), and absolute worst case, respectively. The results are given in Table III. As shown, the error factors are relatively small regardless of the offset distance. Also, as expected, the errors increase as d is decreased. This is due to increased coupling between the stub and tuning bars as d is decreased.

TABLE III
SIMULATED LINE-LENGTHENING TUNING STUB ERRORS FOR THREE IMPORTANT CASES.

Alumina

	Frequency	Re[Z _{in}] Error (Ω)	Im[Z _{in}]Error (Ω)	Z _{in} Error (%)
Typical Case: d = 10 mils	10 GHz	0.000	0.127	0.046
	35 GHz	0.000	0.045	0.067
Compact Case: d = 5 mils	10 GHz	-0.001	0.935	0.341
	35 GHz	-0.001	0.328	0.491
Absolute Worst Case: d = 1 mils	10 GHz	-0.008	8.506	3.100
	35 GHz	-0.008	2.900	4.350

Ferro A6M

	Frequency	Re[Z _{in}] Error (Ω)	Im[Z _{in}]Error (Ω)	Z _{in} Error (%)
Typical Case: d = 8 mils	10 GHz	-0.001	0.237	0.075
	35 GHz	0.000	0.083	0.094
Compact Case: d = 4 mils	10 GHz	-0.003	1.595	0.501
	35 GHz	-0.001	0.514	0.629
Absolute Worst Case: d = 2 mils	10 GHz	-0.007	5.009	1.573
	35 GHz	-0.004	1.609	1.969

1. a. TFN Line-Lengthening Tuning Stub Configuration: Distance-from-the-Line Error Analysis

The line-lengthening tuning stub configuration is simulated and the error is determined as the offset distance is increased. Fig. 16 shows the simulated Z_{in} error results for (a) alumina and (b) Ferro A6M at 10, 20, and 35 GHz. For both substrates the tuning bar error exponentially decreases with offset distance and is practically null at $d = 8$ mils. The results show that the errors increase with frequency. This is simply because the electrical length of the tuning bars increases with frequency, resulting in a greater impact on circuit performance. For comparison purposes, the electrical length of the tuning bar on alumina substrate at 10 GHz is 4 degrees while the electrical length at 35 GHz is 14 degrees.

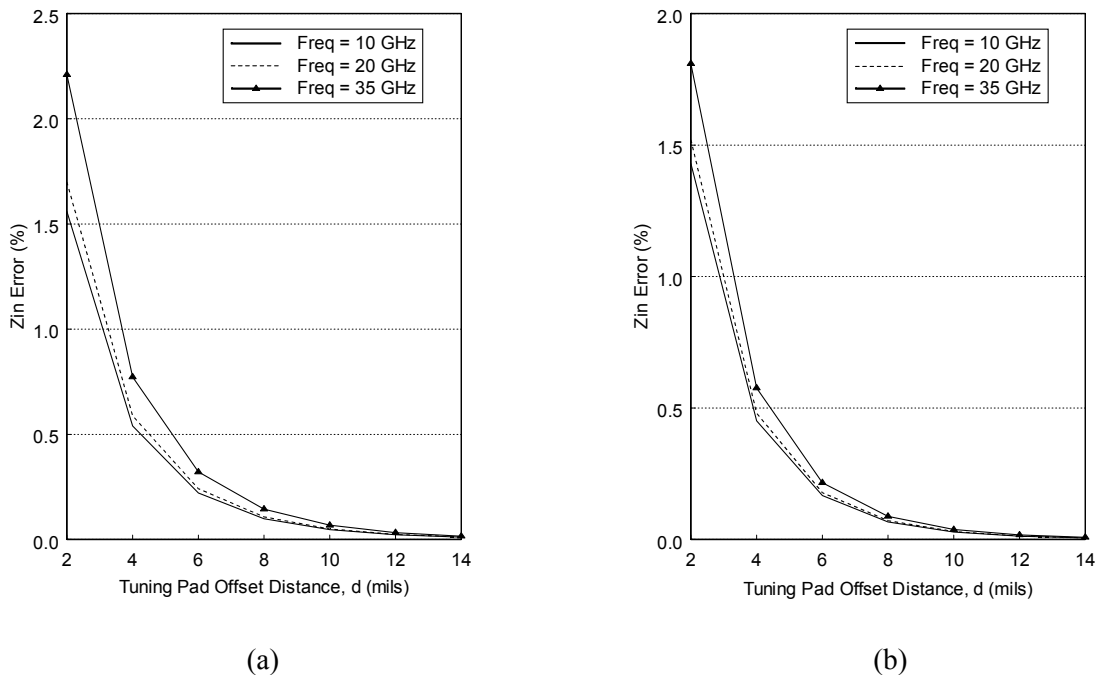


Fig. 16 Simulated error factors for (a) alumina and (b) Ferro A6M. Substrate thickness=10 mils.

1.b. TFN Line-Lengthening Tuning Stub Configuration: Resonant Frequency Error Analysis

In many cases, open stubs are used as resonators in filters and oscillators. To determine the effect of the line-lengthening tuning stub configuration on resonant stubs, resonant circuits with and without line lengthening tuning bars are simulated and the resonant frequency errors are found. Fig. 17 shows the perturbed quarter wave stub resonant circuits that are simulated for alumina substrate. In Fig. 17 (a) the circuit is designed to resonant at 10 GHz and in Fig. 17 (b) the circuit resonates at 35 GHz. The lengths of the quarter wave stub resonant circuits for alumina at 10 and 35 GHz are 115 and 32 mils, respectively.

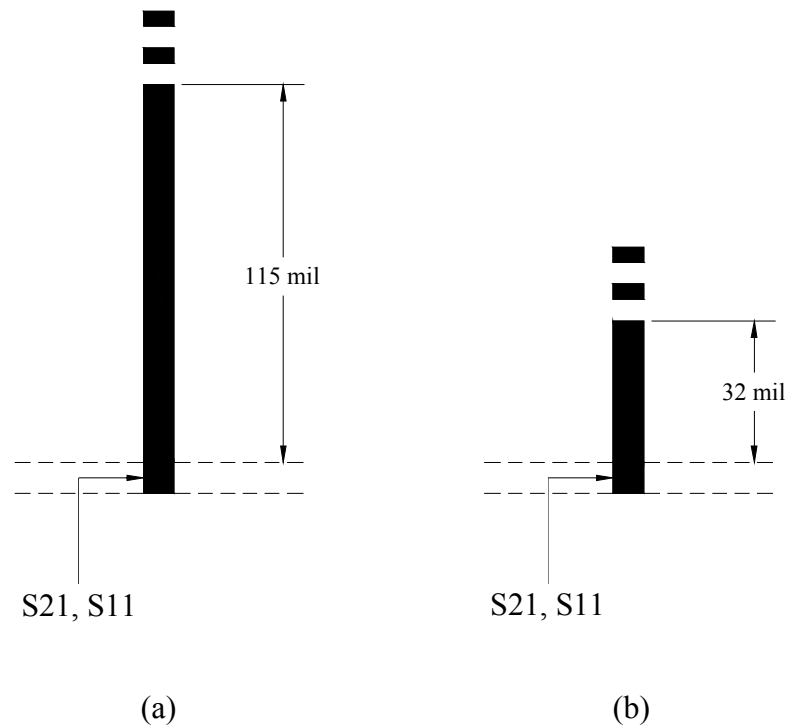


Fig. 17 Quarter wave stub resonant circuit at (a) 10 GHz and (b) 35 GHz with line-lengthening tuning stubs.

The resonant frequency errors for the three cases (typical, compact, and absolute worst case) are given in Table IV. For both alumina and Ferro A6m, the tuning bar error is significant for the compact case at 35 GHz ($> 0.1\%$). The errors are even more significant for the absolute worst case. For example, at 35 GHz the error is almost 1.0 % for the tuning stub configuration on alumina substrate.

TABLE IV
SIMULATED TFN QUARTER WAVE STUB RESONANT FREQUENCY ERROR RESULTS FOR
THREE IMPORTANT CASES.

Alumina

	Approx. Resonant Frequency (GHz)	Resonant Frequency Error (MHz)	Resonant Frequency Error (%)
Typical Case: d = 10 mils	10	Error <1	Error <0.01
	35	-5	-0.014
Compact Case: d = 5 mils	10	-3	-0.03
	35	-40	-0.11
Absolute Worst Case: d = 1 mil	10	-32	-0.32
	35	-335	-0.957

Ferro A6M

	Approx. Resonant Frequency (GHz)	Resonant Frequency Error (MHz)	Resonant Frequency Error (%)
Typical Case: d = 8 mils	10	Error <1	Error <0.01
	35	-5	-0.014
Compact Case: d = 4 mils	10	-3	-0.03
	35	-35	-0.1
Absolute Worst Case: d = 2 mils	10	-12	-0.12
	35	-158	-0.45

2. $6 \times 16 \text{ mil}^2$ Rectangular Tuning Chips in a Cluster (RTCC)

The two common dimensions of the individual tuning bars comprising the TFN RTCC configuration are $6 \times 16 \text{ mil}^2$ and $10 \times 10 \text{ mil}^2$. In this section, the $6 \times 16 \text{ mil}^2$ case is

analyzed, and Fig. 18 shows the general layout of the $6 \times 16 \text{ mil}^2$ RTCC configuration. In practice, there can be more than three columns of tuning bars, more than two rows of bars, and the bars can be on one or both sides of the microstrip thru line.

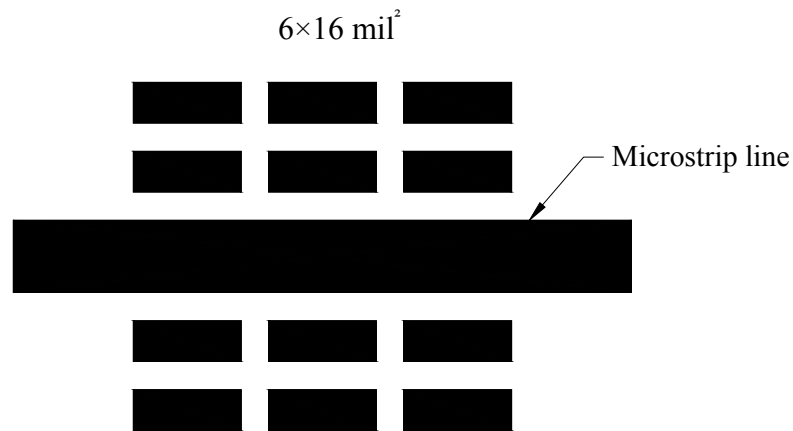


Fig. 18 Typical $6 \times 16 \text{ mil}^2$ TFN RTCC configuration.

When simulating, the feed line is de-embedded as shown in Fig. 19. In the figure, two parallel dashed lines represent the de-embedded feed line. The length of the microstrip thru line for both alumina and Ferro A6M extends 6 mils beyond the tuning bar configuration in both directions to account for fringing fields. The distance between the first row and the thru line is equal to the distance between rows of tuning bars and is denoted d_1 . The distance between the columns of tuning chips is d_2 . Fig. 19 shows the tuning bar pattern arranged in two rows-by-five columns flanking both sides of the line. This thesis analyzes up to a maximum of five columns.

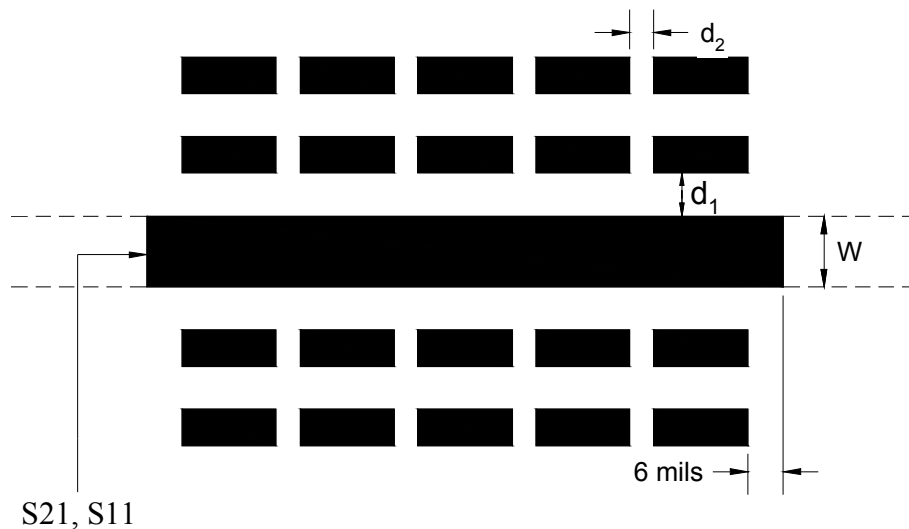
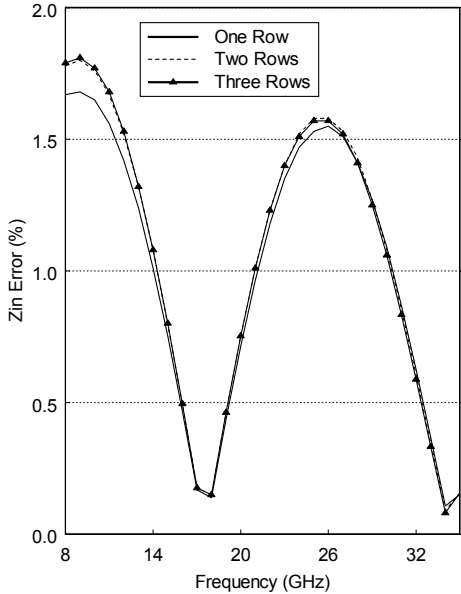


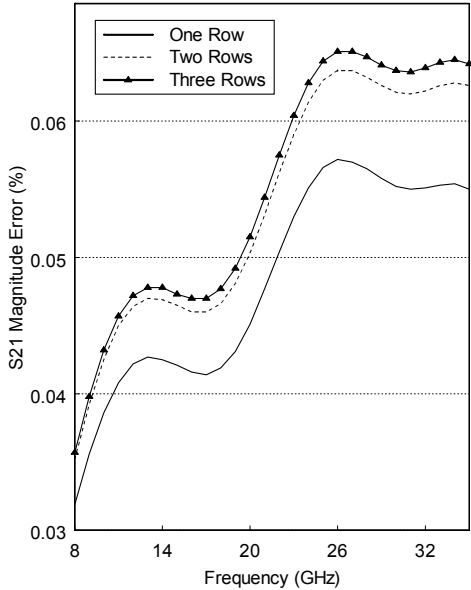
Fig. 19 Geometry of $6 \times 16 \text{ mil}^2$ TFN RTCC configuration analyzed in this thesis.

2.a. $6 \times 16 \text{ mil}^2$ RTCC: Effect of Multiple Rows

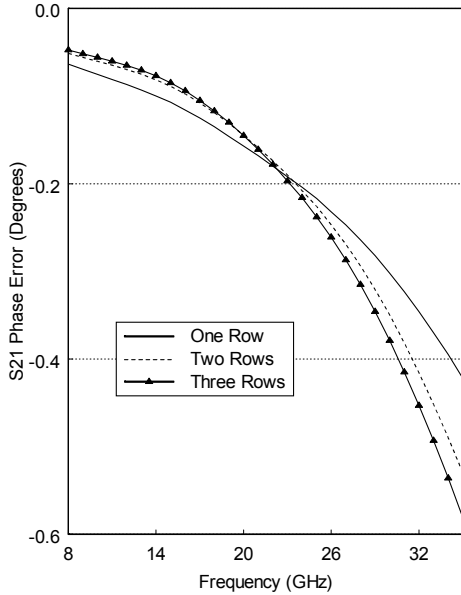
First, the effect of multiple rows of tuning bars on the tuning bar error is investigated. The $6 \times 16 \text{ mil}^2$ RTCC configuration is simulated on alumina containing five columns with one, two, and three rows of tuning bars flanking both sides of the line. This corresponds to three cases; (1) one row-by-five columns flanking both sides, (2) two rows-by-five columns flanking both sides, and (3) three rows-by-five columns flanking both sides. In the simulation, $d_1 = 5 \text{ mils}$, $d_2 = 10 \text{ mils}$, and $\Gamma_0 = 0$ (matched line). Fig. 20 gives the simulated results, where it is seen that the error factors are affected mainly by the first two rows of tuning bars closest to the thru line. Furthermore, the majority of the signal perturbation is caused by only the first row of bars closest to the line. This is similar to the TFN line-lengthening tuning stub configuration, in which it was found that only the first two tuning bars closest to the line need to be taken into account for error analysis (see Fig. 15).



(a)



(b)



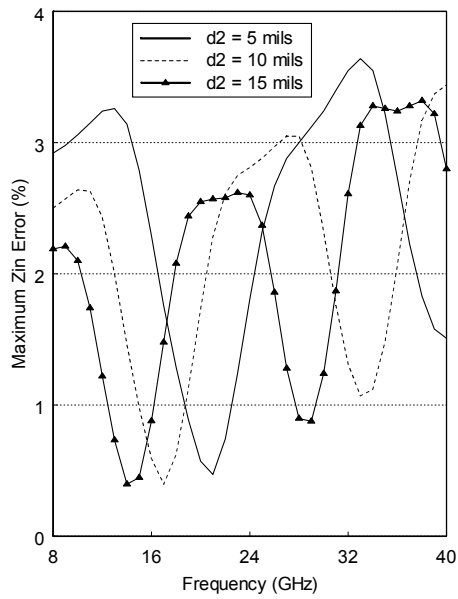
(c)

Fig. 20 Simulated (a) Z_{in} , (b) S21 magnitude, and (c) S21 phase error factors for alumina. Results are for $6 \times 16 \text{ mil}^2$ tuning bars arranged in five columns on both sides of the line with $d_1 = 5 \text{ mils}$, $d_2 = 10 \text{ mils}$, and $VSWR = 1$.

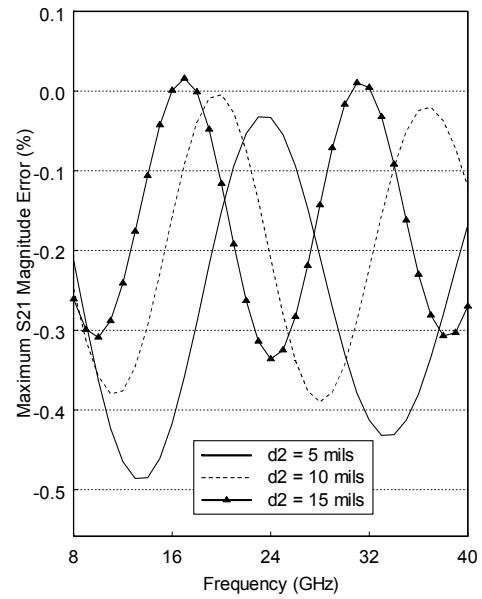
2.b. 6×16 mil² RTCC: *Effect of Distance between Columns (d_2)*

The distance between the columns of tuning bars (d_2) affects mainly the frequency characteristics of the error factor curves. To illustrate this, an error maximization procedure (as discussed in section B.2 of this chapter) is performed on alumina with one row-by-five columns of tuning bars flanking both sides of the line with $d_1 = 4$ mils and $|\Gamma_0| = 1/3$ (VSWR = 2). The simulation results are shown in Fig. 21. As shown in the figure, the maximum (or peak) values of the error factors are relatively close for different values of d_2 . It can also be seen that the error curves oscillate as a function of frequency. The maximum values of the error factors occur approximately at frequencies where the electrical length of the section of line adjacent to the tuning bars is an odd multiple of 90 degrees. To illustrate, for $d_2 = 5$ mils, the total length of line adjacent to the tuning bars is $16 \cdot 5 + 5 \cdot 4 = 100$ mils. This has an electrical length of 90 and 180 degrees at 11.45 and 22.53 GHz, respectively. It can be seen from Fig. 21 that these two frequencies approximately correspond to the maximum and minimum values of the errors, respectively. Therefore, as d_2 is increased, the electrical length of the line increases, and thus the general shape of the error curves shifts to lower frequencies.

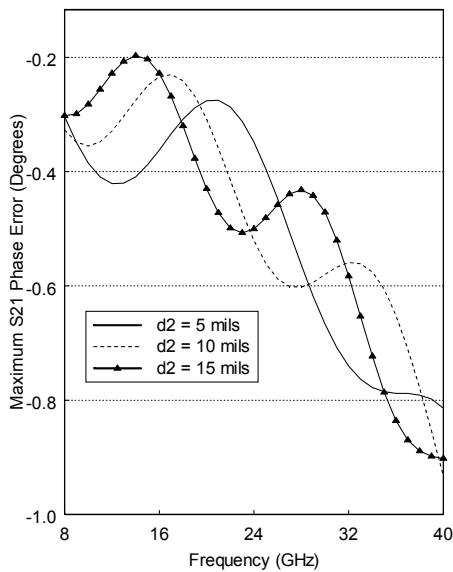
This oscillatory phenomenon can be explained by considering the equivalent circuit of a coupled line section representation. The equivalent circuit of a coupled section is simply an equal length transmission line with characteristic impedance $Z_{0,eq} = (Z_{0e} + Z_{0o})/2$ (see Fig. 9). Therefore the RTCC configuration is equivalent to a transmission line with a characteristic impedance periodically alternating between Z_0 and $Z_{0,eq}$. When the total effective electrical length of the perturbed line for this simple model is 180 degrees, the input impedance approaches the load impedance. Therefore, one would expect little error in this case. When the effective electrical length of the perturbed line is 90 degrees, the line acts similar to a quarter wave transformer and is thus more dependent on the effective perturbation-dependent characteristic impedance. To more exactly explain and predict the response shown in Fig. 21, one would have to take into account the multiple reflections at each junction between segments of transmission line with characteristic impedance Z_0 and $Z_{0,eq}$.



(a)



(b)



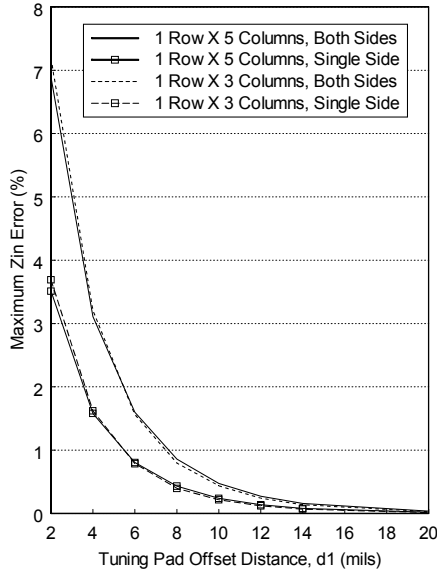
(c)

Fig. 21 Simulated maximum (a) Z_{in} , (b) S_{21} magnitude, and (c) S_{21} phase error factors for alumina. Results are for 6×16 mil² tuning bars arranged as one row-by-five columns on both sides of the line with $d_1=4$ mils and VSWR=2.

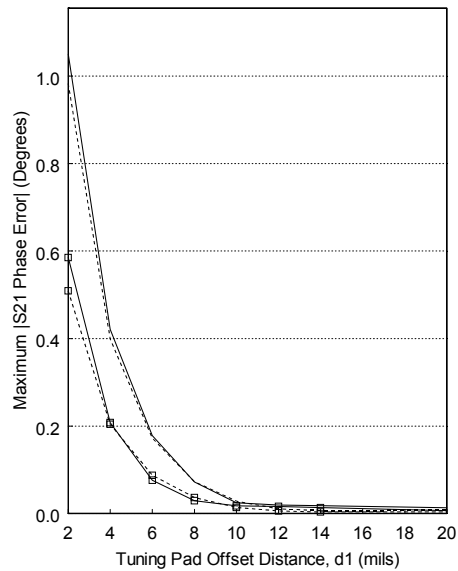
2.c. 6×16 mil² RTCC: Distance-from-the-Line Error Analysis

The 6×16 mil² RTCC configuration involves many variables including the number of rows and columns, row and column offset distances, frequency, load impedance, and layout (whether or not the tuning bars flank one or both sides of the thru line). To simplify the analysis, the following error maximization procedure is performed. First, d_2 is kept at 5 mils for both alumina and Ferro A6M. The tuning bar configuration is then simulated for various offset distances, d_1 . Next the error maximization procedure, as described in the previous section, is performed over a frequency range 8-40 GHz with $|\Gamma_0| = 1/3$ (VSWR = 2). The maximum value of both the Z_{in} and S21 error factors are extracted and plotted versus tuning bar offset distance for the frequency ranges 8-24 GHz and 24-40 GHz.

Figs. 22 and 23 give the simulated results for alumina at 8-24 GHz and 24-40 GHz, respectively. Figs. 24 and 25 give the simulated results for Ferro A6M. The S21 magnitude error factors are negligible and not shown. The results show that the error factors decrease exponentially with offset distance d_1 and are quite small- even at half a substrate height. Also, the errors are higher for the cases where the tuning bars flank both sides compared to the cases where the bars flank a single side. At higher frequencies (8-24 GHz), the errors are greater for the 5 column arrangement compared to the 3 column arrangement. Finally, it can be observed that the errors for the tuning bar configuration on alumina substrate are only slightly larger than that on the Ferro A6M substrate. Yet, when considering the offset distance in terms of percentage of substrate height, the parasitic effects are slightly higher for Ferro A6M than alumina.

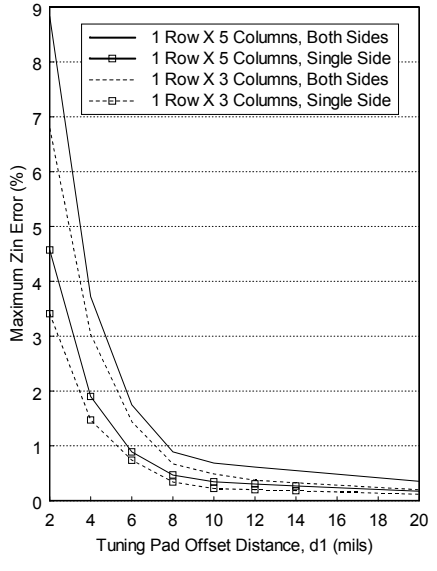


(a)

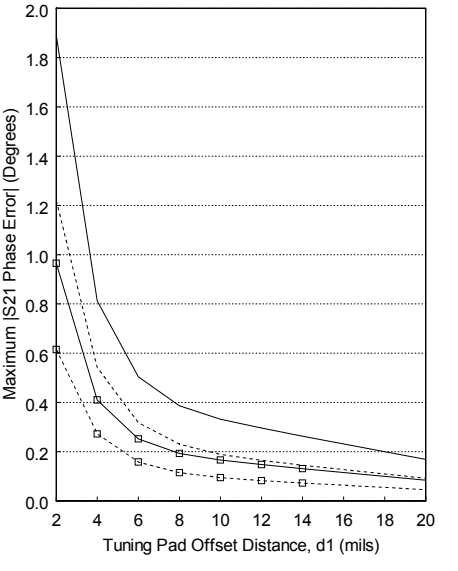


(b)

Fig. 22 Maximum (a) Z_{in} error factors and (b) S_{21} phase error factors for alumina. Results are for 6×16 mil^2 tuning bars with $d_2 = 5$ mils, substrate thickness=10 mils and $\text{VSWR}=2$. Frequency range: 8-24 GHz.

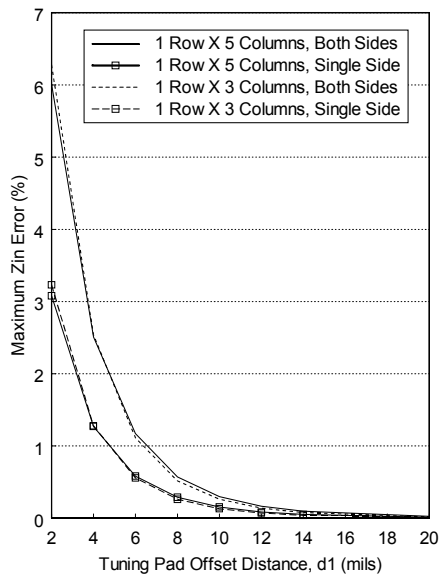


(a)

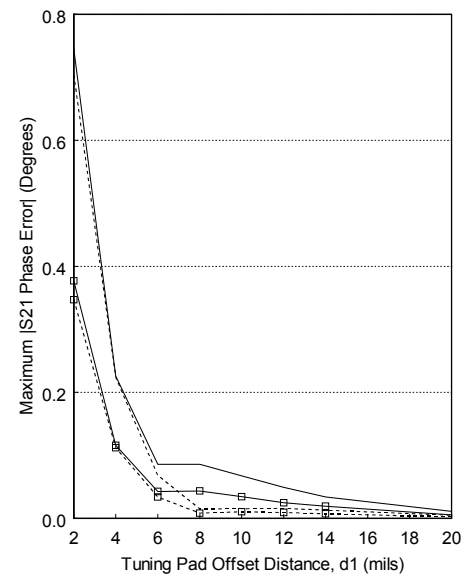


(b)

Fig. 23 Maximum (a) Z_{in} error factors and (b) S_{21} phase error factors for alumina. Results are for 6×16 mil^2 tuning bars with $d_2 = 5$ mils, substrate thickness=10 mils, and $\text{VSWR}=2$. Frequency range: 24-40 GHz.

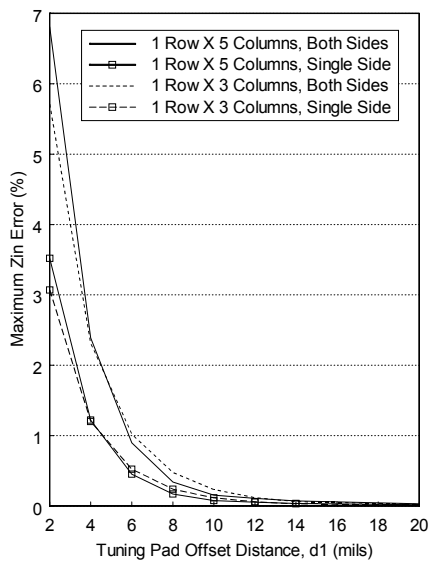


(a)

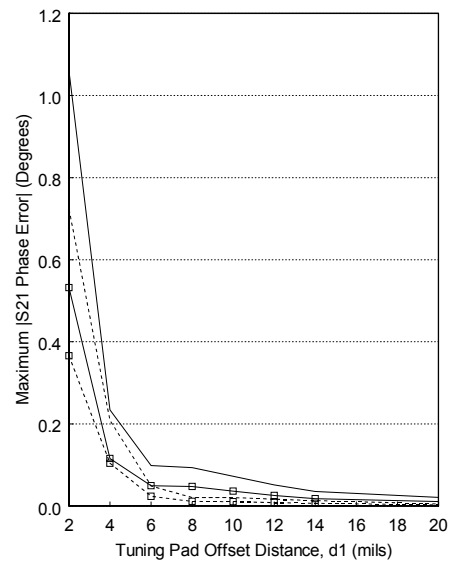


(b)

Fig. 24 Maximum (a) Z_{in} error factors and (b) S_{21} phase error factors for Ferro A6M. Results are for $6 \times 16 \text{ mil}^2$ tuning bars with $d_2 = 5$ mils, substrate thickness = 7.4 mils and VSWR = 2. Frequency range: 8-24 GHz.



(a)



(b)

Fig. 25 Maximum (a) Z_{in} error factors and (b) S_{21} phase error factors for Ferro A6M. Results are for $6 \times 16 \text{ mil}^2$ tuning bars with $d_2 = 5$ mils, substrate thickness = 7.4 mils and VSWR = 2. Frequency range: 24-40 GHz.

3. $10 \times 10 \text{ mil}^2$ RTCC

The previous section analyzed the TFN RTCC configuration comprised of discrete tuning bars each of dimension $6 \times 16 \text{ mil}^2$. The other common dimension of tuning bar used in the TFN RTCC configuration is $10 \times 10 \text{ mil}^2$, which is analyzed in this section. Fig. 26 shows the general layout of the $10 \times 10 \text{ mil}^2$ RTCC configuration. In practice, there can be more than three columns of tuning bars, more than one row of bars, and the bars can be on one or both sides of the microstrip thru line.

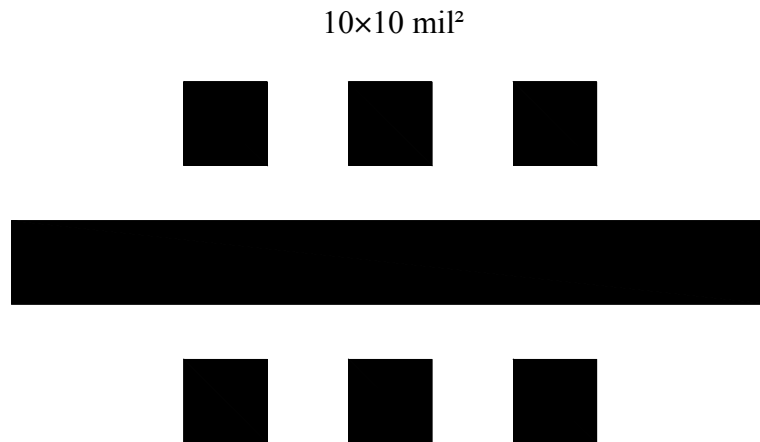
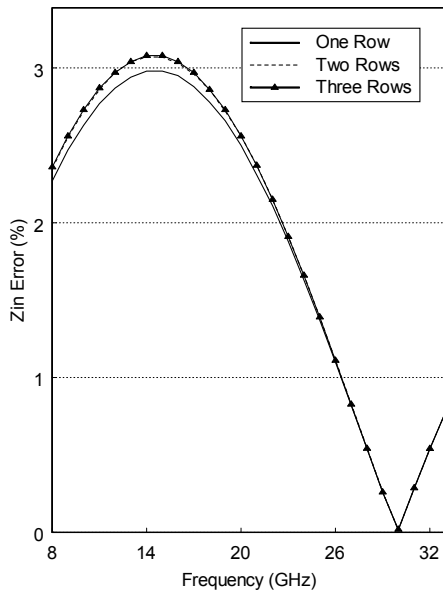


Fig. 26 Typical $10 \times 10 \text{ mil}^2$ TFN RTCC.

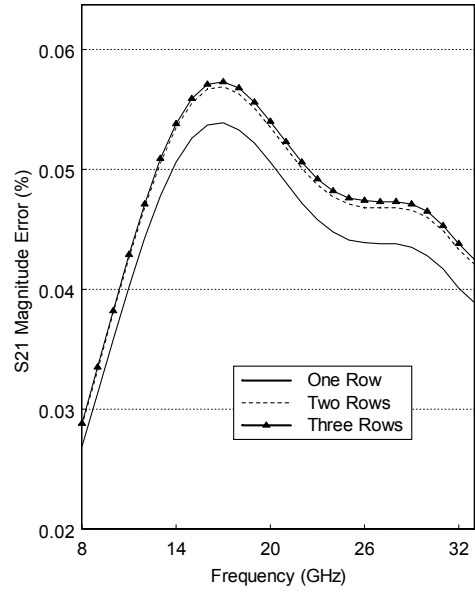
When simulating, the $10 \times 10 \text{ mil}^2$ RTCC is de-embedded in the same manner as the $6 \times 16 \text{ mil}^2$ RTCC; namely, the length of the microstrip thru line for both alumina and Ferro A6M extends 6 mils beyond the tuning bar configuration in both directions to account for any fringing fields. Also, like the $6 \times 16 \text{ mil}^2$ case, the distance between the first row of tuning bars and the microstrip thru line is equal to the distance between rows of bars and is denoted d_1 . The distance between the columns of tuning bars is denoted d_2 .

3.a. 10×10 mil² RTCC: Effect of Multiple Rows

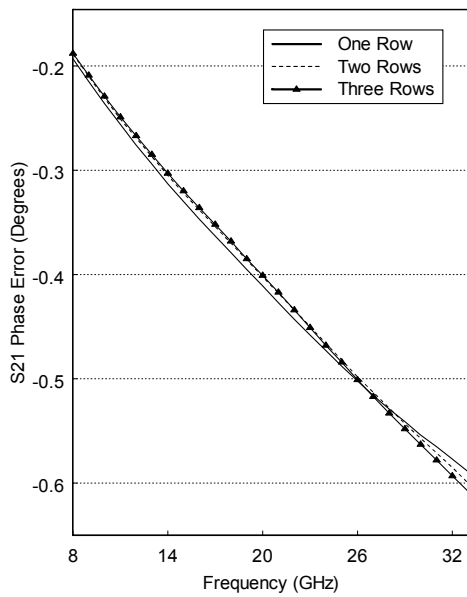
Resembling the 6×16 mil² RTCC configuration, only the first row of 10×10 mil² tuning bars closest to the microstrip thru line cause the majority of the signal perturbation. To illustrate this, the 10×10 mil² RTCC is simulated on alumina containing five columns with one, two, and three rows on both sides of the line. This corresponds to three cases; (1) one row-by-five columns flanking both sides, (2) two rows-by-five columns flanking both sides and (3) three rows-by-five columns flanking both sides. In the simulation, $d_1 = 5$ mils, $d_2 = 10$ mils, and $\Gamma_0 = 0$ (matched line). Fig. 27 gives the simulated error results. It is evident from these results that the second and third rows have almost no effect on the frequency dependence or magnitude of the error factors and parasitic coupling. Therefore, the results of the error analysis determined through the simulation of one row can be safely applied to the cases comprising multiple rows. The reason is because only the tuning bars directly adjacent to the thru line couple energy from the line. This concept is similar to that when designing microwave filters using coupled resonators. That is, one usually only considers the coupling between adjacent resonators in the filter, which in turn keeps the coupling matrix as sparse as possible and simplifies the problem.



(a)



(b)

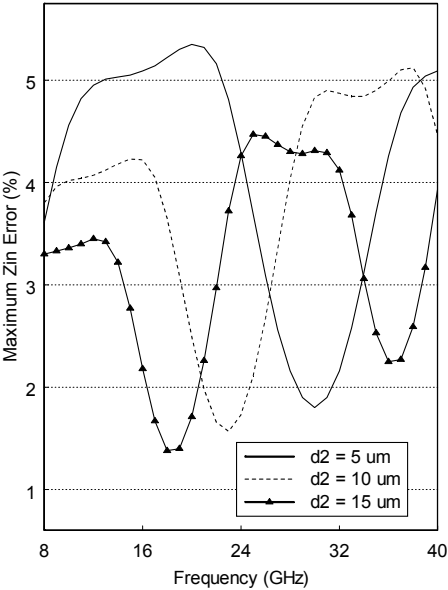


(c)

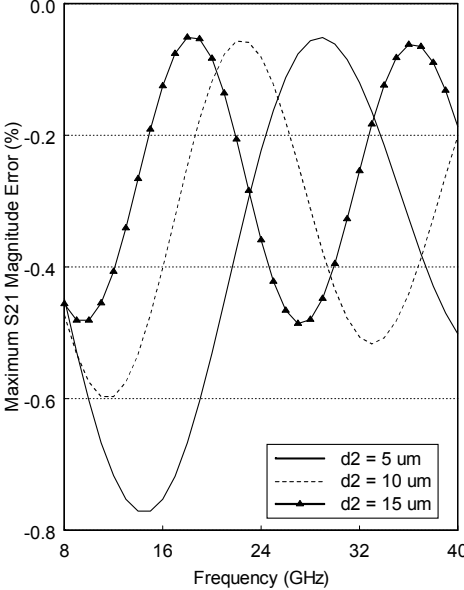
Fig. 27 Simulated (a) Z_{in} , (b) S_{21} magnitude, and (c) S_{21} phase error factors for alumina. Results are for 10×10 mil² tuning bars arranged in five columns on both sides of the line with $d_1=5$ mils, $d_2=10$ mils, and VSWR=1.

3.b. $10 \times 10 \text{ mil}^2$ RTCC: Effect of Distance between Columns (d_2)

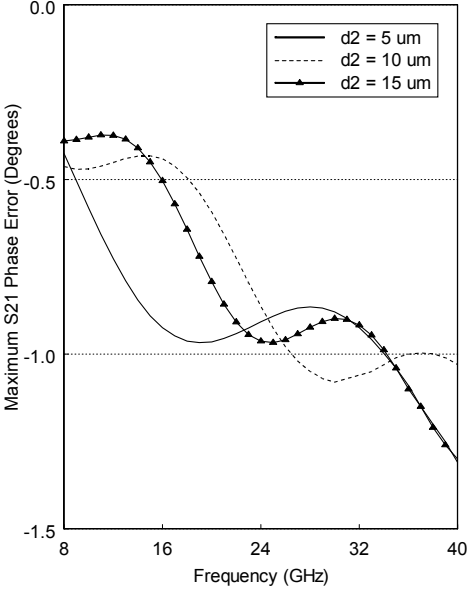
Also, similar to the $6 \times 16 \text{ mil}^2$ RTCC configuration, the distance between the columns of tuning bars d_2 affects mainly the frequency characteristics of the error factor curves. To demonstrate this, an error maximization procedure is performed on alumina with the $10 \times 10 \text{ mil}^2$ tuning bars arranged as one row-by-five columns flanking both sides of the line, $d_1=4$ mils, and $|\Gamma_0| = 1/3$ (VSWR=2). The simulation results are shown in Fig. 28. As shown in the figure, the maximum (or peak) values of the error factors are relatively close for different values of d_2 . Like the $6 \times 16 \text{ mil}^2$ RTCC configuration, the error curves oscillate as a function of frequency, and the maximum values of the error factors occur approximately at frequencies where the electrical length of the section of line adjacent to the tuning bars is an odd multiple of 90 degrees. The minimum values of the error factors occur approximately at frequencies where the electrical length of the section of line adjacent to the tuning bars is an even multiple of 90 degrees. This oscillatory behavior was also observed for the $6 \times 16 \text{ mil}^2$ RTCC configuration and was explained in section C.2.b of this chapter by considering the equivalent circuit of a coupled line representation. Essentially, when the total effective electrical length of the perturbed line is 180 degrees, the input impedance approaches the load impedance, and one would expect little error. When the effective electrical length of the perturbed line is 90 degrees, the line acts similar to a quarter wave transformer and would thus exhibit a higher error compared to the unperturbed case.



(a)



(b)



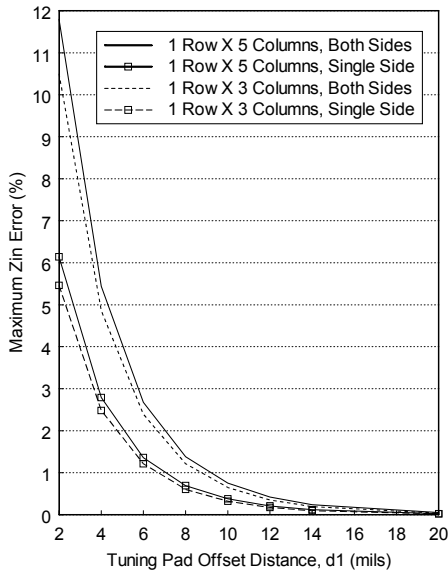
(c)

Fig. 28 Simulated maximum (a) Z_{in} , (b) S21 magnitude, and (c) S21 phase error factors for alumina. Results are for $10 \times 10 \text{ mil}^2$ tuning bars arranged as one row-by-five columns on both sides of the line with $d_1=4 \text{ mils}$ and $VSWR=2$.

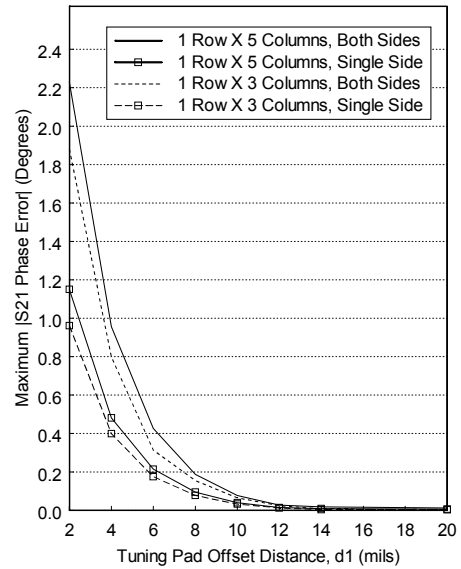
3.c. 10×10 mil² RTCC: Distance-from-the-Line Error Analysis

The same error maximization procedure is performed on the 10×10 mil² RTCC as the 6×16 mil² case. Namely, the tuning bar configuration is simulated for various offset distances d_1 over a frequency range 8-40 GHz with $|\Gamma_0| = 1/3$. Then the maximum values of the Z_{in} and S21 phase errors are extracted. Figs. 29 and 30 give the simulated results for alumina at 8-24 GHz and 24-40 GHz, respectively. Figs. 31 and 32 give the simulated results for Ferro A6M. The S21 magnitude error factors are negligible and not shown.

The distance-from-the-line error analyses findings for both the 6×16 mil² and 10×10 mil² RTCC show the error factors exponentially decreases with frequency. Furthermore the error factors are similar for both alumina and Ferro A6M. In general the S21 phase error is less than 1 degree for an offset distance d_1 of half a substrate height. These results not only confirm the validity of placing tuning bars a distance of one substrate height (in this case the substrate thickness is 10 mils for alumina and 7.4 mils for Ferro A6M) from the line to achieve negligible error, but show this convention is rather conservative for many instances. The errors for the 10×10 mil² cases are also comparatively larger than the corresponding 6×16 mil² cases. It is therefore apparent that the width of the tuning bars has more of an adverse effect on circuit performance than the length of the bar (at least for the range of dimensions considered here). This is similar to the error analysis findings from the tuning bar configuration on GaAs substrate, where it was found that the errors increase for a decreasing characteristic impedance (increasing width).

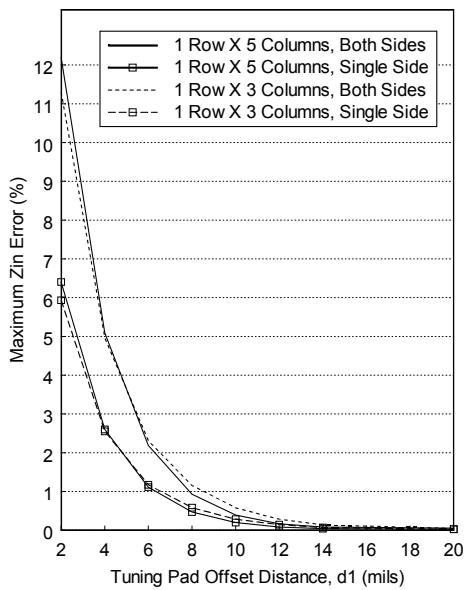


(a)

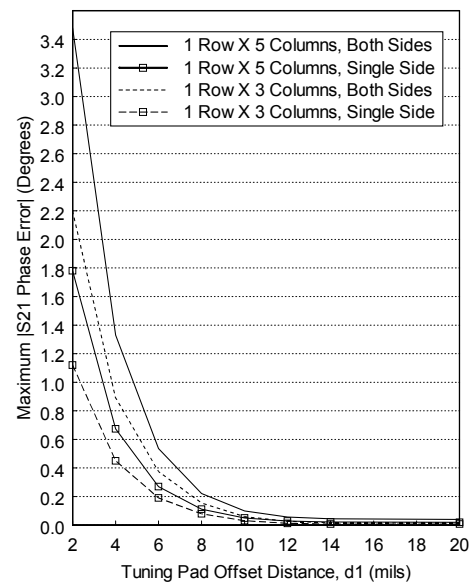


(b)

Fig. 29 Maximum (a) Z_{in} error factors and (b) S_{21} phase error factors for alumina. Results are for 10×10 mil^2 tuning bars with $d_2 = 5$ mils, substrate thickness=10 mils and VSWR=2. Frequency range: 8-24 GHz.



(a)



(b)

Fig. 30 Maximum (a) Z_{in} error factors and (b) S_{21} phase error factors for alumina. Results are for 10×10 mil^2 tuning bars with $d_2 = 5$ mils, substrate thickness=10 mils and VSWR=2. Frequency range: 24-40 GHz.

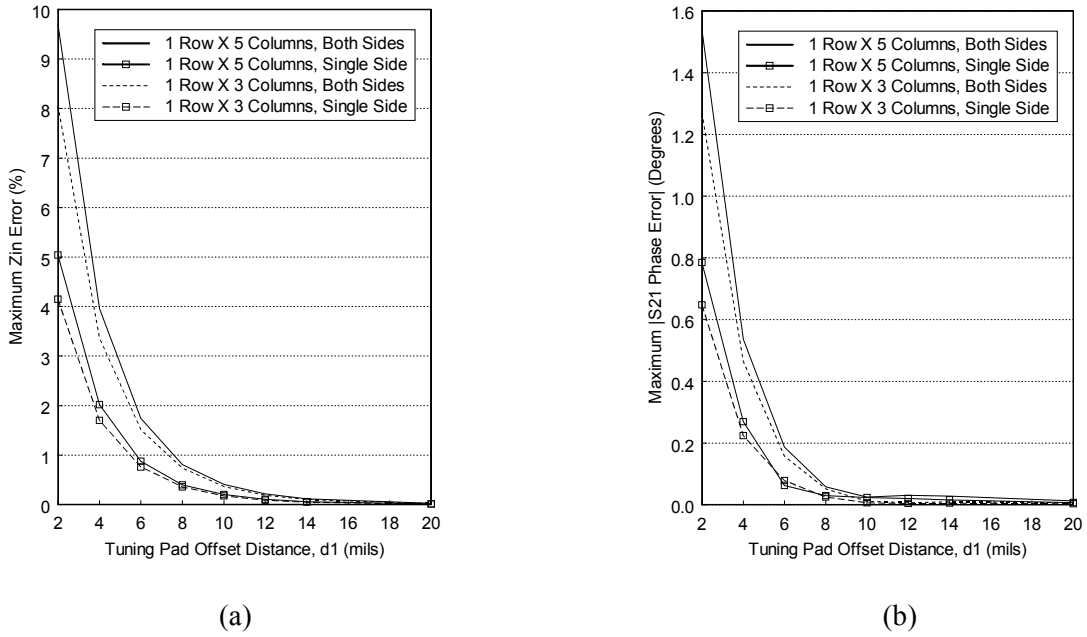


Fig. 31 Maximum (a) Z_{in} error factors and (b) S21 phase error factors for Ferro A6M. Results are for $10 \times 10 \text{ mil}^2$ tuning bars with $d_2 = 5 \text{ mils}$, substrate thickness=7.4 mils and VSWR=2. Frequency range: 8-24 GHz.

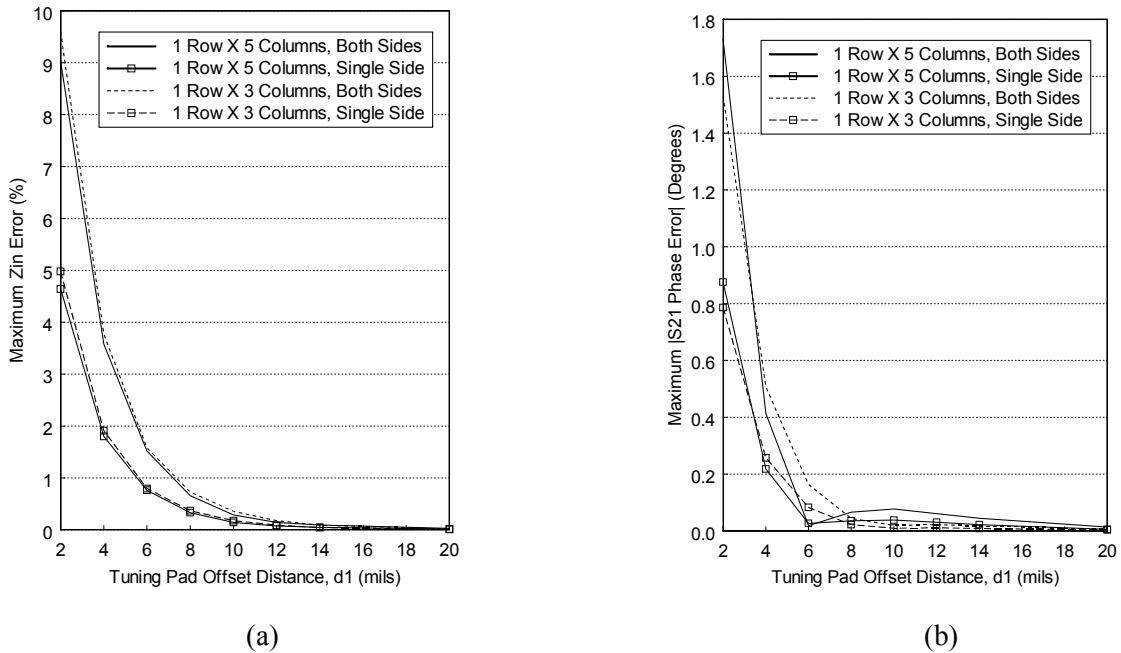


Fig. 32 Maximum (a) Z_{in} error factors and (b) S21 phase error factors for Ferro A6M. Results are for $10 \times 10 \text{ mil}^2$ tuning bars with $d_2 = 5 \text{ mils}$, substrate thickness=7.4 mils and VSWR=2. Frequency range: 24-40 GHz.

4. Mismatched Lines with High VSWR

The standing waves resulting from highly mismatched loads can lead to higher tuning bar errors than given in the preceding analyses. This is due to the relatively high coupling that exists between voltage and current maximums in the thru line and adjacent tuning bars. Thus far in this thesis the largest VSWR analyzed is 2, because most microwave circuits in post-production have low mismatches. Yet, there may be cases with high load mismatch, and caution should be taken regarding tuning bar placement.

After many simulations with various load reflection coefficients it was found that the TFN RTCC error is most sensitive to load mismatch compared to the other tuning bar configurations (including the GaAs MMIC tuning bar configurations). It is therefore recommended that the RTCC configurations be placed at points in the circuit with low mismatch. If this cannot be done then d_2 (the distance between columns of tuning bars) can be designed so that a minimum tuning bar error falls within the frequency of interest (see Fig. 28), or at the very least, the tuning bar offset distance d_1 should be greater than one substrate height.

5. Conclusions

In this section the error due to the TFN line-lengthening tuning stub configuration and the RTCC configuration is analyzed for both alumina and Ferro A6M substrates. A distance-from-the-line error analysis as well as a resonant frequency error analysis shows that the line-lengthening tuning bars can be placed closer than one substrate height – especially for lower frequencies. For both the line-lengthening configuration and RTCC configuration, the tuning bars placed directly adjacent to the microstrip line cause the majority of the error. Also, the RTCC configuration error is sensitive to not only the distance between rows d_1 but also the distance between columns d_2 . A distance-from-the-line error analysis is provided for both the 6×16 mil² and 10×10 mil² RTCC configurations for various cases, and assists the design of compact tuning bar configurations with minimum parasitic effects. Finally, it should be noted that higher

mismatch loads lead to higher tuning bar errors due to the increased coupling between the tuning bars and thru line.

D. Measurements and Experimental Validation

To demonstrate the accuracy of Sonnet and the simulation settings used in this chapter, measurements are made on microstrip quarter-wave stub resonators and compared to simulated results. The resonators are fabricated on Duroid 6010.5 using the etching facilities available at the Department of Electrical Engineering at Texas A&M University and measured on the Hewlett-Packard 8510C Network Analyzer.

1. Circuit Layout

An open circuit quarter-wave stub resonant circuit is fabricated on Duroid 6010.5 ($\epsilon_r = 10.5$) with a substrate height of 10 and 25 mils, and the exact replicas are simulated using Sonnet. The circuit layout for the resonator (a) without tuning bars and (b) with tuning bars is shown in Fig. 33 for a substrate height h of 10 mils. The 10×10 mil² tuning bars are arranged in two vertical columns with five rows flanking both sides of the line. The offset distances between both rows and columns of tuning bars are equal to 8 mils (minimum distance allowed due to fabrication tolerances). For the resonator with $h = 25$ mils, the tuning bars are arranged as described above, except, due to the increased substrate height, the dimensions of the bars are 24×24 mil² to preserve the ratio between substrate height and tuning bar dimensions.

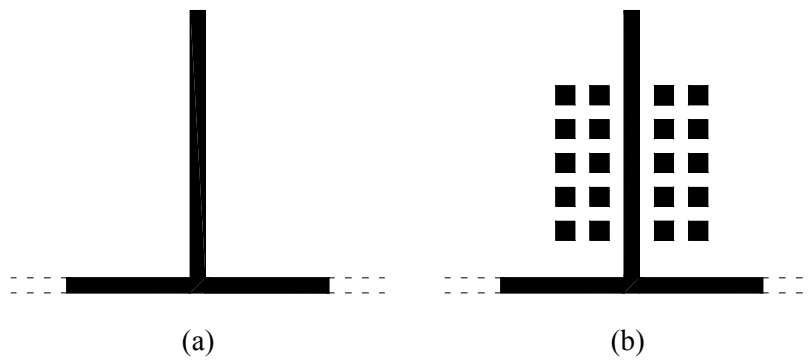
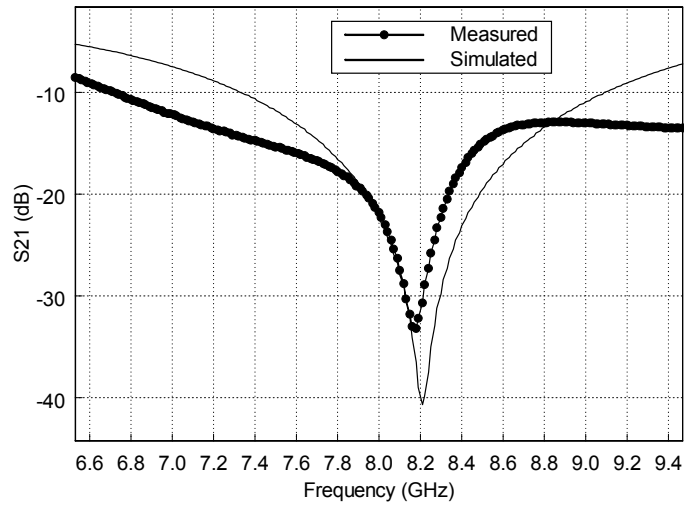


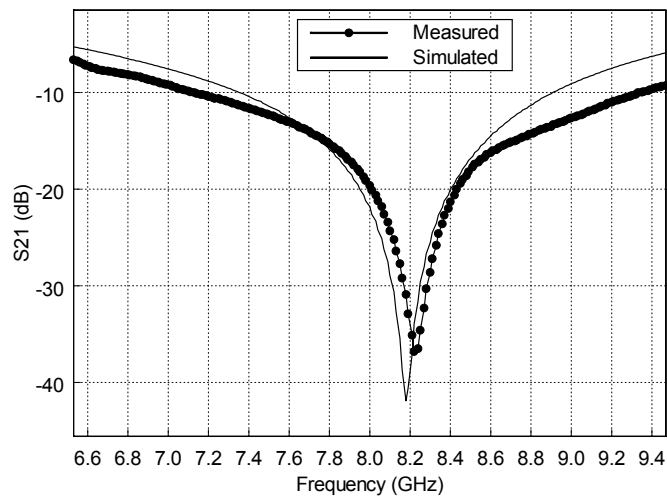
Fig. 33 Layout of measured stub resonator (a) with and (b) without tuning bars. $\epsilon_r = 10.5$, $h = 10$ mils. *Note:* $50\ \Omega$ feedlines extend farther than shown.

2. Measurements

Fig. 34 shows the measured and simulated S_{21} curves for the simple resonator without the tuning bars for (a) $h=10$ mils and (b) $h=25$ mils. For both substrate heights, the measured and simulated results agree quite well, with the resonant frequencies differing by only about 15 MHz. Also, as expected, the insertion loss is higher for the measured set due to connector losses and mismatch and non-ideal metallization effects (such as conductor surface roughness).



(a)



(b)

Fig. 34 Simulated vs. measured S21 curve of a stub resonator for (a) $h=10$ mils and (b) $h=25$ mils. $\epsilon_r=10.5$.

The (a) measured and (b) simulated S21 curves for the resonator with and without the tuning bars are shown in Fig. 35 for $h = 10$ mils and Fig. 36 for $h = 25$ mils.

For both cases, the simulation agrees in general with the measured resonant frequency shift caused by the tuning bars. To accurately measure such a small effect, the resonant circuit with tuning bars is first measured. Then, with the circuit still connected to the test fixture, the tuning bars are carefully removed using a fine blade and microscope, and the resulting resonant circuit, void of tuning bars, is measured a second time. It can be observed that the frequency shift is larger in the measurements as compared to that in simulation. This may be due to a discrepancy between conductor thickness, offset distance, or dielectric constant between the circuit simulated (and expected) and that actually fabricated.

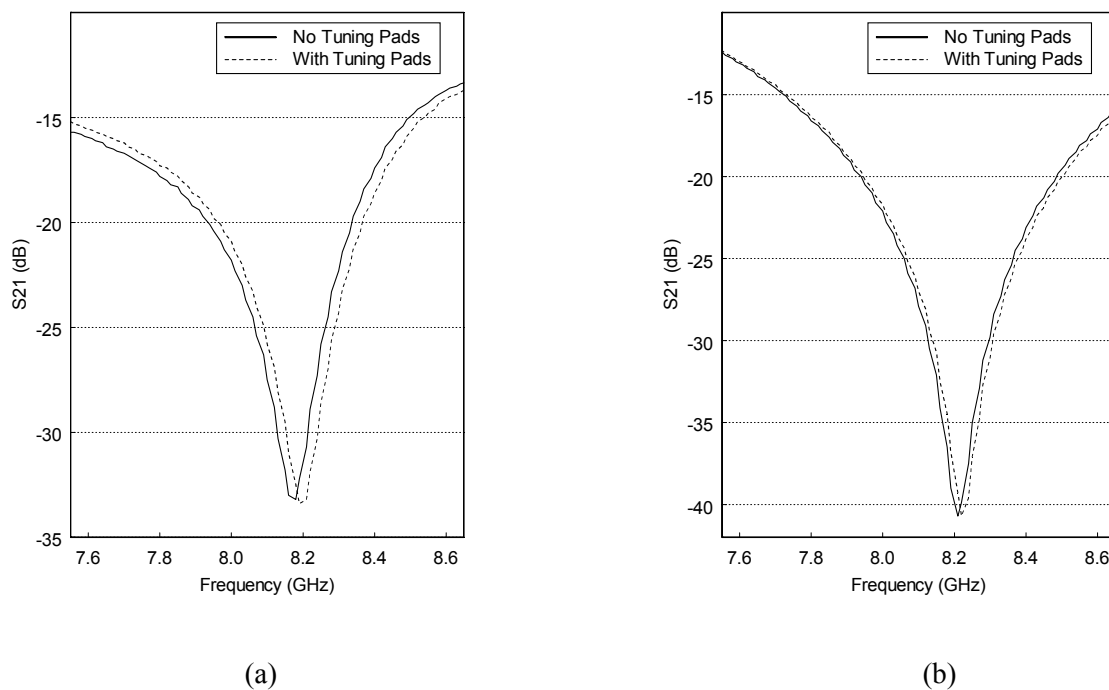


Fig. 35 (a) Measured and (b) simulated resonant circuit with and without the tuning bars. $\epsilon_r=10.5$, $h=10$ mils.

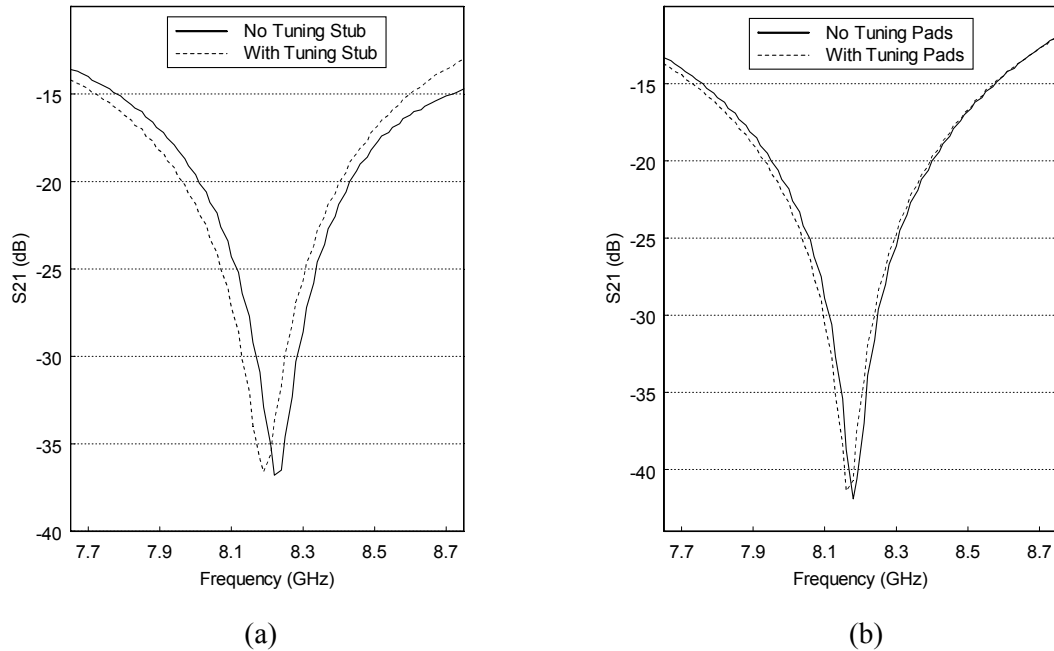


Fig. 36 (a) Measured and (b) simulated resonant circuit with and without the tuning bars. $\epsilon_r=10.5$, $h=25$ mils.

3. Conclusions

In this section, the accuracy of Sonnet to simulate the effect of unused tuning bars was demonstrated by comparing both measurement and simulation of a quarter-wave open stub resonator with and without tuning bars. Sonnet accurately predicted the resonant frequency of the quarter-wave stub as well as the small resonant frequency shift caused by the tuning bars. The same general Sonnet simulation settings used to simulate in this section are used throughout the chapter.

E. Recommendations and Conclusions

1. Summary

Microwave circuit designs frequently employ tuning bars to allow the impedance or length of a microstrip line to be adjusted in post production. In GaAs MMIC design,

the tuning configuration is comprised of an airbridge with a single rectangular or horseshoe-shaped tuning bar adjacent to the main thru line. In MMIC module (or TFN) design, both the line-lengthening tuning stub and rectangular tuning chip configurations are used. The line-lengthening tuning stub configuration consists of multiple rectangular bars offset at the end of an open microstrip line, and the rectangular tuning chip configuration consists of rectangular metal patterns flanking the main thru line.

To nullify the parasitic effects of the tuning bars, conventional wisdom suggests placing the bars 1.0 to 1.5 substrate heights away from the main line. While successful in the past, this practice may not result in the most efficient and cost-effective placement of tuning bars in today's compact microwave circuits. This thesis facilitates the design of compact tuning pad configurations with minimum parasitic effects by analyzing the error attributable to GaAs MMIC and alumina/Ferro A6M TFN tuning pad configurations with parameters and offset distances specified by Raytheon.

The error factors of the tuning bar configurations, which characterize the deviation from the unaffected case in the transmission of a signal along the perturbed line, were determined by electromagnetic simulations using Sonnet. After the lines with and without tuning pads were simulated in Sonnet, the resulting S-parameters were imported into ADS, where ADS's optimization capabilities were employed to find the maximum tuning pad error factors for a specified VSWR and frequency. The accuracy of these simulations was verified through experimental measurements.

This thesis not only validates the conventional practice of placing tuning bars 1.0 to 1.5 substrate heights away from the main line, but for many cases finds this practice to be quite conservative. For example, the GaAs MMIC tuning bar configuration has a very small effect on circuit performance even when the tuning bar is only half a substrate height away from the main thru line. Also, in general, the parasitic effects of the tuning bars decrease exponentially with offset distance. Finally, highly mismatched loads result in higher tuning bar parasitic effects due to increased coupling between thru line and the tuning bars. This phenomenon was found most prominent for the TFN rectangular tuning chip configuration.

2. Recommendations

To achieve a negligible effect, recommended tuning bar offset distances are given in this section based on this chapter's error analysis findings with $VSWR \leq 2$. The criterion for "negligible effect" is chosen so that the error factors, Z_{in} and S21 magnitude error, are less than ~1% and the S21 phase error is less than 1 degree. Note that if $VSWR > 2$ then the recommendations may not hold, because, in general, the parasitic effects of the tuning bars increases as the load mismatch increases.

Table V gives the recommended offset distances for both the rectangular and U-shaped (horseshoe-shaped) GaAs MMIC tuning bars. As Table V shows, the lower the characteristic impedance (the wider the line), the greater the tuning bar offset distance should be. Also, the rectangular shaped tuning bars can safely be placed closer to the thru line than the U-shaped bars. The recommendations are based on a substrate height of 100 μm , a rectangular tuning bar length less than 200 μm , and a U-shaped tuning bar inner radius equal to 50 μm .

Both the TFN line lengthening and rectangular tuning chip configurations were analyzed for alumina (substrate height = 10 mils) and Ferro A6M (substrate height = 7.4 mils). Overall, the parasitic effects of the tuning bars were just slightly higher for Ferro A6M than alumina when considering the offset distance in terms of percentage of substrate height. Table VI gives the recommended offset distances for the line-lengthening tuning stub configuration.

TABLE V
RECOMMENDED GAAS MMIC TUNING BAR OFFSET DISTANCES.

Rectangular-shaped

Z_0 (Ω)	Frequency Band	Recommended Offset Distance (% of Substrate Height)
25	X,Ku,K	55
	Ka	65
50	X,Ku,K	45
	Ka	60
100	X,Ku,K	<30
	Ka	<30

U-shaped

Z_0 (Ω)	Frequency Band	Recommended Offset Distance (% of Substrate Height)
25	X,Ku,K	70
	Ka	80
50	X,Ku,K	55
	Ka	70
100	X,Ku,K	<30
	Ka	<30

TABLE VI
RECOMMENDED TFN LINE-LENGTHENING TUNING STUB OFFSET DISTANCES.

Substrate	Frequency Band	Recommended Offset Distance (% of Substrate Height)
Alumina	X,Ku,K	55
	Ka	65
Ferro A6M	X,Ku,K	65
	Ka	80

Table VII gives the recommended offset distances for the TFN rectangular tuning chip configuration with tuning bar dimensions $6 \times 16 \text{ mil}^2$ and $10 \times 10 \text{ mil}^2$. Comparatively, the $10 \times 10 \text{ mil}^2$ tuning bars cause higher signal perturbation and should be placed farther from the thru line. Recommendations are based on the case comprising of one row-by-five columns with a column spacing of 5 mils. Simulation results indicate that multiple rows have little effect, since tuning bars directly adjacent to the thru line cause the majority of the parasitic effects. Therefore, these recommendations hold for rectangular tuning chip configurations with more than one row of tuning bars.

TABLE VII
RECOMMENDED TFN RECTANGULAR TUNING CHIP CONFIGURATION OFFSET DISTANCES.

Tuning Bar Dimensions: 6 × 16 mil²

Substrate	Layout	Frequency Band	Recommended Offset Distance (% of Substrate Height)
Alumina	Single Side	X,Ku,K Ka	60 70
	Double Side	X,Ku,K Ka	80 85
Ferro A6M	Single Side	X,Ku,K Ka	70 70
	Double Side	X,Ku,K Ka	90 95

Tuning Bar Dimensions: 10 × 10 mil²

Substrate	Layout	Frequency Band	Recommended Offset Distance (% of Substrate Height)
Alumina	Single Side	X,Ku,K Ka	75 75
	Double Side	X,Ku,K Ka	95 95
Ferro A6M	Single Side	X,Ku,K Ka	80 80
	Double Side	X,Ku,K Ka	100 100

CHAPTER III

COMPACT RESONATORS USING THE TRANSMISSION LINE APPROACH OF NEGATIVE REFRACTIVE INDEX METAMATERIALS*

A. Introduction

Electromagnetic wave propagation through periodic structures has been extensively studied for decades [9] with various applications in microwaves and optics such as masers, traveling-wave tubes, microwave filter networks, phase shifters, antennas, and photonic band gap structures [8], [10]. In the 1950's and 1960's, lattices of discrete metallic elements were applied to the design of lightweight microwave antenna lenses [11]. Because the periodic spacing and element dimensions are on a scale much smaller than a wavelength, these so-called artificial dielectrics can be considered an effective medium. Accordingly, the macroscopic electromagnetic properties of the structures can be described by an effective electric permittivity and magnetic permeability. Recently artificial composite materials exhibiting a *negative* effective permittivity and permeability have been developed. Such a medium, also referred to as a negative refractive index (NRI) medium, was first realized using an array of metal posts and split-ring resonators [12],[13]. Since then, other realizations of NRI media have been developed by various means such as using embedded magnetodielectric spherical particles [14] and L-C loaded transmission lines [15].

In 1968, Veselago first theoretically investigated the electrodynamics of a medium with a simultaneous negative real permittivity and permeability [16]. He described such materials as “left-handed” since the electric field \mathbf{E} , magnetic field \mathbf{H} ,

*Part of the data reported in this chapter is reprinted with permission from “Compact gap coupled resonator using negative refractive index microstrip line” by A.D. Scher, C.T. Rodenbeck, and K. Chang, 2004. *Electronics Letters*, vol. 40, pp. 126-127. Copyright 2004 by The Institution of Electrical Engineers (IEE).

and wave vector \mathbf{k} form a left-handed triplet as opposed to a right-handed triplet for ordinary materials. Consequently, in this medium the phase velocity is opposite to the direction of power flow, and all phenomena connected to the phase of the wave is reversed including a reversed Doppler shift and backward Cherenkov radiation [16], [17]. Additionally, the medium has a negative index of refraction – a defining characteristic of media exhibiting both a negative permittivity and permeability [18]. The renewed interest in NRI media stems from the work of Pendry [19]-[21] as well as the first direct measurement of a negative index of refraction [16] confirming Veselago's original predictions over three decades later.

To quantitatively demonstrate the counterintuitive phenomena associated with an NRI medium, consider first a lossless electromagnetic dielectric with real permittivity ϵ and real permeability μ . The Maxwell curl equations are

$$\nabla \times \mathbf{E} = -j\omega\mu\mathbf{H} \quad (6)$$

$$\nabla \times \mathbf{H} = j\omega\epsilon\mathbf{E} \quad (7)$$

Solving the curl equations (6) and (7) for the E and H field vectors of a plane wave in the usual manner gives

$$\mathbf{E} = \mathbf{E}_0 \exp(-j\mathbf{k} \cdot \mathbf{r}) \quad (8)$$

$$\mathbf{H} = \frac{1}{\omega\mu} (\mathbf{k} \times \mathbf{E}_0) \exp(-j\mathbf{k} \cdot \mathbf{r}) \quad (9)$$

where \mathbf{E}_0 is the polarization vector. Substituting (8) and (9) into (6) and (7) gives

$$\mathbf{k} \times \mathbf{E} = j\omega\mu\mathbf{H} \quad (10)$$

$$\mathbf{k} \times \mathbf{H} = -j\omega\epsilon\mathbf{E} \quad (11)$$

For a conventional medium with positive μ and ϵ , (10) and (11) mean the vectors \mathbf{k} , \mathbf{E} , and \mathbf{H} form a right-handed triplet, and, consequently, \mathbf{k} points in the direction of power flow as given by the Poynting vector \mathbf{S} where

$$\mathbf{S} = \mathbf{E} \times \mathbf{H} \quad (12)$$

Yet it also follows from (10) and (11) that if both μ and ϵ are negative, the wave vector \mathbf{k} turns in the opposite direction and \mathbf{k} , \mathbf{E} , and \mathbf{H} form a left-handed set [16]. This means the phase velocity of the plane wave is opposite to the direction of power flow. In the cases where only one of the μ or ϵ is negative and the other positive, \mathbf{k} is imaginary and the wave does not propagate [17].

To illustrate the concept of negative refraction, consider a uniform plane wave incident upon a dielectric interface between a conventional medium M1 ($\epsilon_{M1}, \mu_{M1} > 0$) and a backward-wave medium M2 ($\epsilon_{M2}, \mu_{M2} < 0$) as shown in Fig. 37. The wavevectors for medium M1 and M2 are \mathbf{k}_1 and \mathbf{k}_2 , respectively. Snell's law requires that the tangential wavevector components \mathbf{k}_{y1} and \mathbf{k}_{y2} must equal across the interface. Furthermore, the conservation of energy requires that the normal components of the Poynting vectors \mathbf{S}_1 and \mathbf{S}_2 remain in the same direction (i.e. the positive x-direction in Fig. 37) for both media. Because M2 is a backward-wave medium, \mathbf{k}_{x2} is antiparallel to the x-component of \mathbf{S}_2 . Therefore, it follows that \mathbf{k}_2 is directed towards the interface and the power is refracted through a negative angle to the normal as shown in Fig. 37 [16].

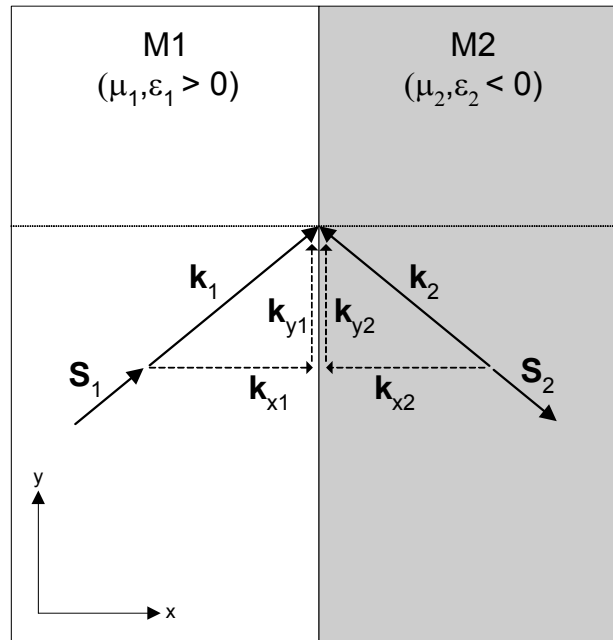


Fig. 37 An NRI medium refracts an incident plane wave at a negative angle with the surface normal.

B. The Transmission Line Approach to NRI Metamaterials

At nearly same time, two independent research groups, one at UCLA and the other at the University of Toronto, introduced the transmission line (TL) approach of NRI metamaterials [22], [23]. In this approach either one or two-dimensional planar NRI media can be realized by periodically loading a transmission line with series capacitors and shunt inductors. The TL approach has several inherent advantages including being both low-loss and broadband [15]. Additionally, it lends itself well for fabrication using established planar circuit technologies such as microstrip. By means of tuning the phase response of the loaded TL, this approach has lead to improvements in conventional RF/microwave circuit designs. Examples include branch-line couplers operating at two arbitrary frequencies [24], broadband compact hybrid couplers [25], and broadband compact phase shifters [26]. While this chapter only analyzes the one-

dimensional NRI TL structure, the concepts involved are easily extendable to two-dimensions [27], [28].

The one-dimensional composite NRI TL unit cell is shown in Fig. 38. The structure consists of a conventional host TL (such as a microstrip line) symmetrically loaded with discrete lumped components, L_N and C_N . The host TL, composed of two segments, has a total length d , a characteristic impedance $Z_0 = \sqrt{L/C}$, and propagation constant $\beta_{TL} = \omega\sqrt{LC}$ where L and C are the TL inductance and capacitance per unit length, respectively.

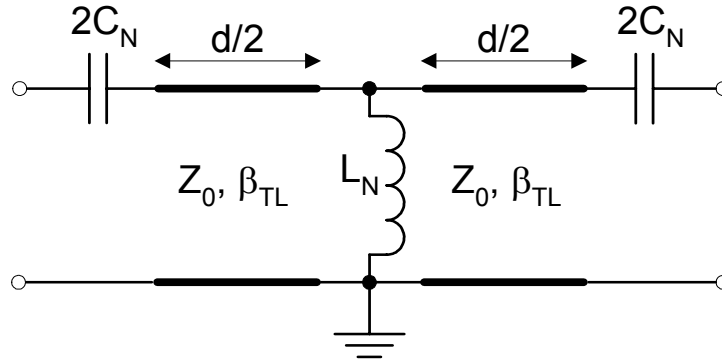


Fig. 38 One-dimensional composite NRI TL unit cell.

The complete dispersion relation for the NRI TL is determined in the well-known manner by computing the [ABCD] matrix of the unit cell and applying Bloch-Floquet periodic boundary conditions [15]

$$\begin{aligned} \cos(\beta_{Bloch}d) = & \cos(\beta_{TL}d) \left(1 - \frac{1}{4\omega^2 L_N C_N} \right) \\ & + \sin(\beta_{TL}d) \left(\frac{1}{2\omega C_N Z_0} + \frac{Z_0}{2\omega L_N} \right) - \frac{1}{4\omega^2 L_N C_N} \end{aligned} \quad (13)$$

where β_{Bloch} is the Bloch propagation constant and $\beta_{TL} = \omega\sqrt{LC}$ is the propagation constant of the host TL. Homogeneity requires that both the physical length of the TL and the phase shift per unit cell be sufficiently small ($\beta_{TL}d \ll 2\pi$ and $\beta_{\text{Bloch}}d \ll 2\pi$). When the homogeneity conditions are met, the dispersion relation of (13) can be simplified and solved for the Bloch propagation constant β_{Bloch} which is also considered the medium's effective propagation constant β_{eff} [29]

$$\beta_{\text{eff}} \approx \pm \omega \sqrt{\left(L - \frac{1}{\omega^2 C_N d} \right) \left(C - \frac{1}{\omega^2 L_N d} \right)} \quad (14)$$

In a similar manner (i.e. by computing the [ABCD] matrix of the unit cell and applying Bloch-Floquet periodic boundary conditions) the medium's effective characteristic impedance Z_{eff} can be defined under the homogeneity conditions

$$Z_{\text{eff}} \approx \sqrt{\frac{\left(L - \frac{1}{\omega^2 C_N} \right)}{\left(C - \frac{1}{\omega^2 L_N} \right)}} \quad (15)$$

Having both β_{eff} and Z_{eff} we can now define the effective permittivity ϵ_{eff} and permeability μ_{eff} for this medium as [29]

$$\epsilon_{\text{eff}} = \frac{\beta_{\text{eff}}}{\omega Z_{\text{eff}}} = C - \frac{1}{\omega^2 L_N} \quad (16)$$

$$\mu_{\text{eff}} = \frac{\beta_{\text{eff}} Z_{\text{eff}}}{\omega} = L - \frac{1}{\omega^2 C_N} \quad (17)$$

The negative root for β_{eff} in (14) is chosen for frequencies where $\varepsilon_{eff}, \mu_{eff} < 0$. This occurs at frequencies less than the eigenfrequency f_{c1} where [30]

$$f_{c1} = \min\left(\frac{1}{2\pi\sqrt{LC_N}}, \frac{1}{2\pi\sqrt{L_N C}}\right) \quad (18)$$

The positive root for β_{eff} in (14) is chosen for frequencies where $\varepsilon_{eff}, \mu_{eff} > 0$. This occurs at frequencies greater than the eigenfrequency f_{c2} where [30]

$$f_{c2} = \max\left(\frac{1}{2\pi\sqrt{LC_N}}, \frac{1}{2\pi\sqrt{L_N C}}\right) \quad (19)$$

In the frequency range $f_{c1} < f < f_{c2}$, β_{eff} is purely imaginary and the structure presents a stopband (analogous to an evanescent mode in a lossless waveguide). This stopband can be closed by equating f_{c1} and f_{c2} corresponding to the following matching condition [15]

$$Z_0 = \sqrt{\frac{L}{C}} = \sqrt{\frac{L_N}{C_N}} \quad (20)$$

Under this condition, the effective propagation constant β_{eff} of (14) simplifies to

$$\beta_{eff} \approx \omega\sqrt{LC} + \frac{-1}{\omega\sqrt{L_N C_N} d} \quad (21)$$

This expression reveals that under matched conditions, the effective propagation constant of the composite NRI TL is the sum of the propagation constants of the host TL and an ideal L-C backward-wave line.

The complete dispersion relation of (13) is plotted in Matlab using the program *nri_tl_displot.m* which is included in Appendix A. The program numerically evaluates the right hand side (RHS) of (13) for a given frequency set and parameters. When the RHS is unity or less, a passband exists and $\beta_{Bloch}d$ is solved by taking inverse cosine of the RHS. When the RHS is greater than unity, a stopband exists, resulting in a gap in the dispersion diagram. Figs. 39 and 40 show the dispersion diagrams for an unmatched ($Z_0 \neq \sqrt{L_N/C_N}$) and matched ($Z_0 = \sqrt{L_N/C_N}$) NRI TL unit cell, respectively. For both cases the host TL has a characteristic impedance $Z_0 = 50 \Omega$ and an electrical length $d = 0.176$ radians (10 degrees) at 1 GHz. In the unmatched case the lumped element values are $L_N = 10$ nH and $C_N = 8$ nH. In the matched case the lumped element values are $L_N = 15$ nH and $C_N = 6$ nH.

The dispersion diagram for the unmatched case shown in Fig. 39 reveals a band structure with two distinct stopbands and passbands. The first stopband exists for frequencies below the cutoff frequency $f_b = 1/(\pi\sqrt{L_N C_N})$ [15] and is due to the high-pass nature of the loaded TL. The first passband occurs at $f_b < f < f_{c1}$. This passband supports *backward waves* [15], meaning the group velocity $v_g = d\omega/d\beta$ is opposite to the phase velocity $v_p = \omega/\beta$ [31]. Thus, for power flow in the positive z direction, the group velocity will be positive while the phase velocity (and consequently β) is negative. This is the NRI band where $\epsilon_{eff}, \mu_{eff} < 0$ and where the negative root for β_{eff} in (14) is chosen. As discussed previously, a stop band exists for $f_{c1} < f < f_{c2}$. As the frequency increases beyond f_{c2} , the effects of the lumped elements decrease and the phase velocity approaches the phase velocity of the host TL [30]. This is the positive refractive index (PRI) band where $\epsilon_{eff}, \mu_{eff} > 0$ and where the positive root for β_{eff} in (14) is selected as in the case for a conventional unloaded TL. For the matched case, as

shown in Fig. 40, the stopband is closed and a seamless transition exists between the NRI and PRI regions. The transition frequency f_0 between the NRI and PRI regions occurs when $\beta_{eff} = 0$ and is given by $f_0 = 1/(2\pi\sqrt{LC}) = 1/(2\pi\sqrt{L_N C_N})$ [30]

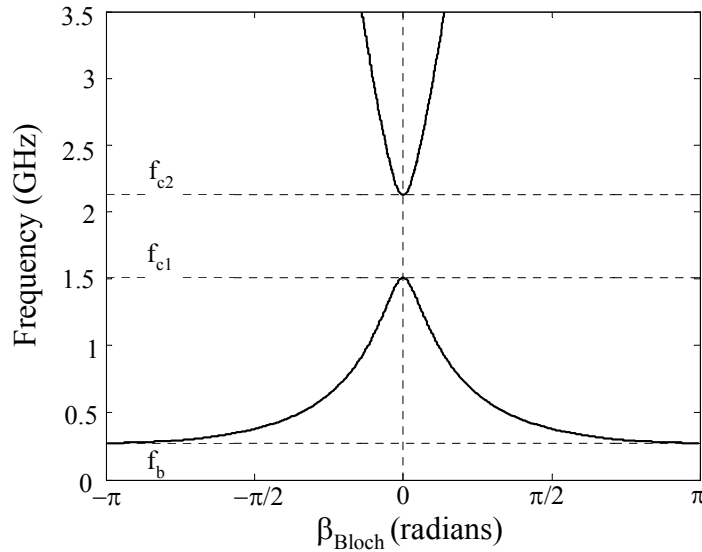


Fig. 39 Dispersion diagram for the NRI TL of Fig. 38 for the unmatched case $\sqrt{L_N/C_N} \neq Z_0$.

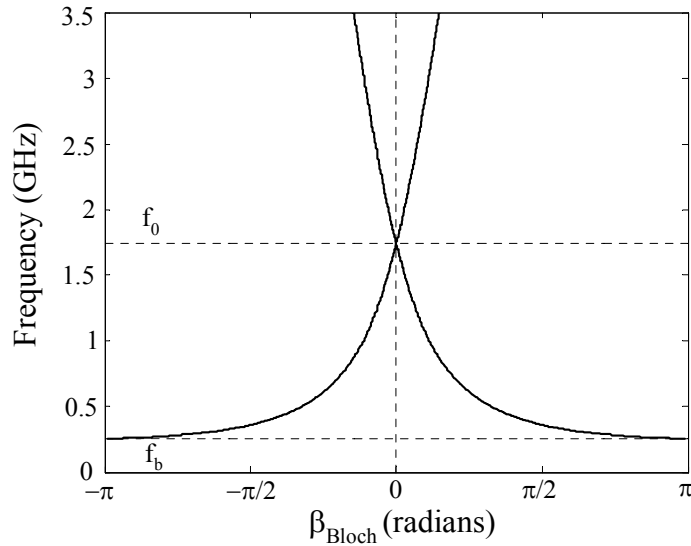


Fig. 40 Dispersion diagram for the NRI TL of Fig. 38 for the matched case $\sqrt{L_N/C_N} = Z_0$.

In general, the dispersion relation of (13) has an infinite number of solutions given by [32]

$$\beta_n = \beta_0 + \frac{2n\pi}{d}, \quad n = 0, \pm 1, \pm 2, \dots \quad (22)$$

where β_n is propagation constant of the n th mode or harmonic and β_0 is the fundamental propagation constant of the wave. This is a universal property of axially periodic structures and is governed by Floquet's Theorem. It follows that wave propagation through periodic structures can be regarded as a superposition of an infinite number of waves with different phase velocities $v_n = \omega / \beta_n$ which get numerically smaller for larger values of n [32]. Each traveling wave (called *space harmonics* or *Hartree harmonics* [33]) has an appropriate coefficient or amplitude governed by the boundary conditions. The effects of spatial harmonics on the operating characteristics of the NRI TL have only begun to be studied in detail [34]. However, we know the higher order spatial harmonics are usually only significant near band edges, which are characterized by points on the dispersion diagram with zero slope corresponding to the onset of a stop band [35]. Consequently, the single dominant mode $n = 0$ is sufficient to accurately describe the field for the matched periodic NRI TL in the passband — especially under homogeneity conditions.

C. Compact Zeroth-Order Resonators Using NRI Microstrip Line

Zeroth-order gap coupled line and ring resonators using NRI microstrip line are designed based on the theory presented in the previous section and experimentally measured. The resonators are considered “zeroth order” because at resonance the effective electrical length of the artificial NRI line is zero. The concept of designing subwavelength resonators using NRI metamaterials was first theoretically investigated in [36] for a general 1-D cavity resonator. The work presented here goes further by detailing the design and measurement of two practical implementations of subwavelength resonators on microstrip using the TL approach of NRI metamaterials.

Compared to conventional resonators, the proposed resonators provide the advantages of harmonic suppression and considerable size reduction.

1. Line Resonators [37]

Fig. 41 shows a schematic diagram of the proposed gap coupled line resonator. The resonator is constructed with a single composite PRI/NRI TL unit cell having an effective electrical length (net phase shift) $\beta_{\text{eff}}l$ of zero degrees at resonance where l is the net length of the resonator. This is achieved through the use of (21) by designing the NRI TL phase advance to equal to the PRI TL phase lag under the matching conditions specified by (20). The resonator is designed for a resonant frequency of 1.2 GHz and fabricated on RT/Duroid 5870 substrate with a thickness of 0.508 mm (20 mils) and a dielectric constant of 2.23. Panasonic surface mount chip capacitors ($1.0 \times 0.5 \text{ mm}^2$) and inductors ($1.6 \times 0.8 \text{ mm}^2$) are used in the design of the gap coupled loaded TL which consists of conventional 50Ω microstrip PRI TLs on each side of a single NRI TL cell. The gap size is 0.2 mm. The NRI TL cell is implemented symmetrically with two series capacitors of value 12 pF and one shunt inductor of value 15 nH. The total length of the PRI microstrip TLs is 10.21 mm resulting in an overall resonator length of 12.09 mm. For comparison, the length of a conventional gap coupled line half-wavelength resonator at 1.2 GHz is 88.14 mm.

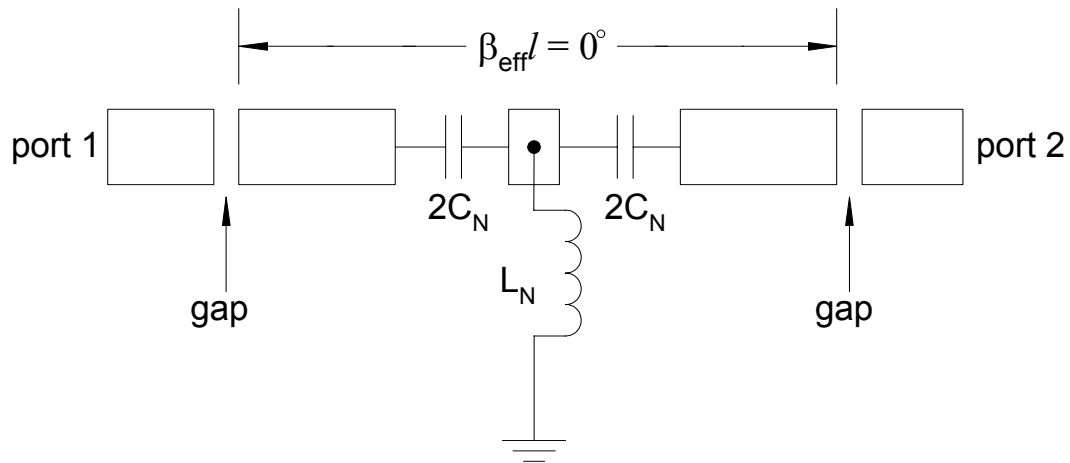


Fig. 41 Schematic diagram of the zeroth order NRI gap coupled line resonator

The proposed PRI/NRI line resonator and a conventional gap coupled resonator are measured using a using an Agilent 8510C network analyzer. Fig. 42 shows a photograph of the fabricated conventional and proposed PRI/NRI gap coupled resonators. The size of the proposed resonator is 86% more compact than that of the conventional one. Measurement results are shown in Fig. 43. The proposed resonator suppresses higher order frequency harmonics up to about 6.5 GHz. Past 6.5 GHz the self-resonant frequency of the lumped components limit the operation of the resonator. The measured loaded Q of the conventional resonator is 132 and the Q of the proposed resonator is 48. As expected, the Q for the lumped inductor, which equals approximately 50 at 1.2 GHz, bounds the Q of the proposed resonator. Therefore, if a higher Q is required, a lower loss inductor should be used.

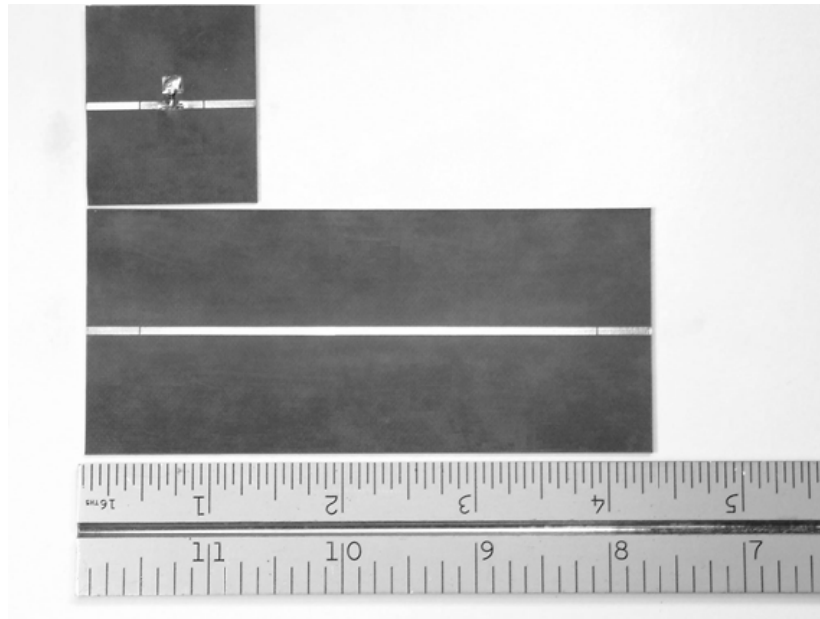


Fig. 42 Photograph of the proposed line resonator circuit (top) compared to a conventional gap coupled resonator (bottom) at 1.2 GHz.

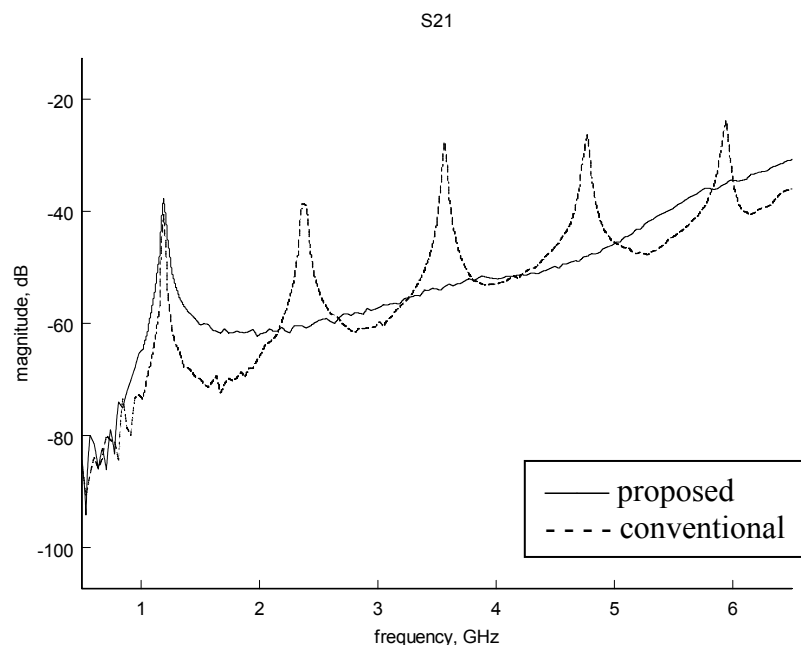


Fig. 43 Measured results for proposed and conventional gap coupled line resonators

2. Ring Resonators

Fig. 44 shows the layout of the compact ring resonator containing a single NRI unit cell. To reduce the curvature effect of the microstrip line, the resonator is implemented using a rectangular loop with chamfered corners. The NRI TL unit cell consists of a section of the microstrip line symmetrically loaded with two series capacitors each of value $2C_N$ and one shunt inductor of value L_N . Like the line resonator, the values of C_N and L_N for the ring resonators are designed to satisfy the matching conditions given in (20). Shown below in Fig. 44 (b) is a rectangular loop. At resonance, the total effective electrical length (net phase delay) of the closed loop is zero degrees and occurs when $\theta_L = -\theta_U$ where θ_U and θ_L are the phase delays for the upper and lower paths, respectively. This condition for resonance is illustrated in Fig. 44 (b).

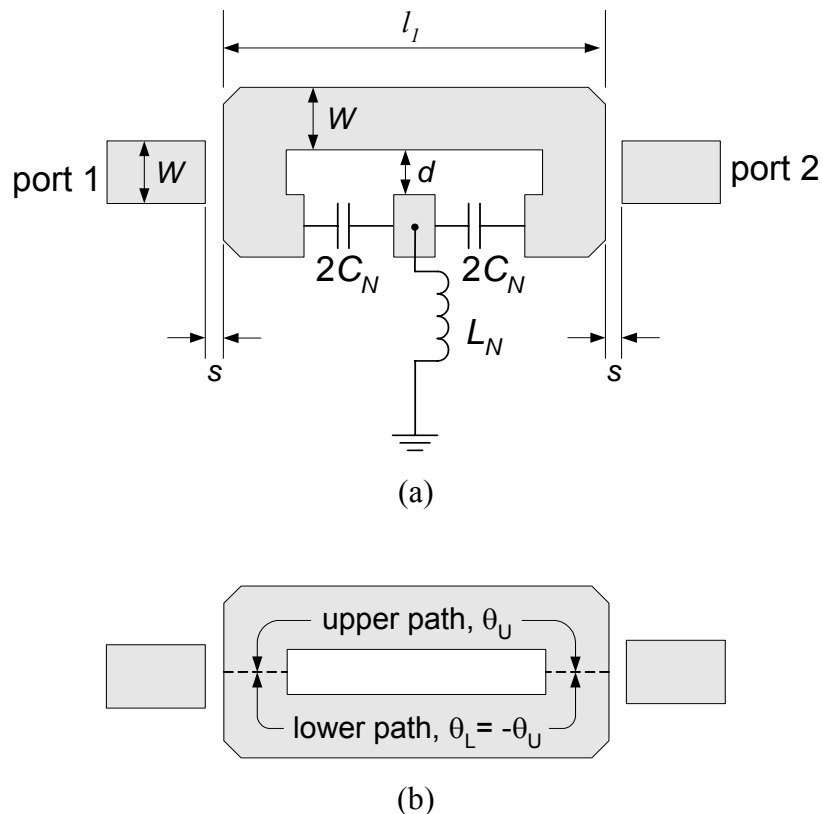


Fig. 44 (a) Layout and (b) condition for resonance for ring resonator using an NRI TL section

The proposed ring structure also resonates even with an inner diameter of zero. The layout of the resonator for this case is shown in Fig. 45 and has the same structure as that in Fig. 44 devoid of chamfered corners and with zero interior area. While not having the conventional ring shape, this resonator is still considered a ring resonator in that at resonance it satisfies the same condition as the NRI ring resonator with an inner diameter greater than zero. Namely, at resonance the phase delay of the upper path θ'_U equals the phase advance of the lower path $-\theta'_L$ as illustrated in Fig. 45 (b).

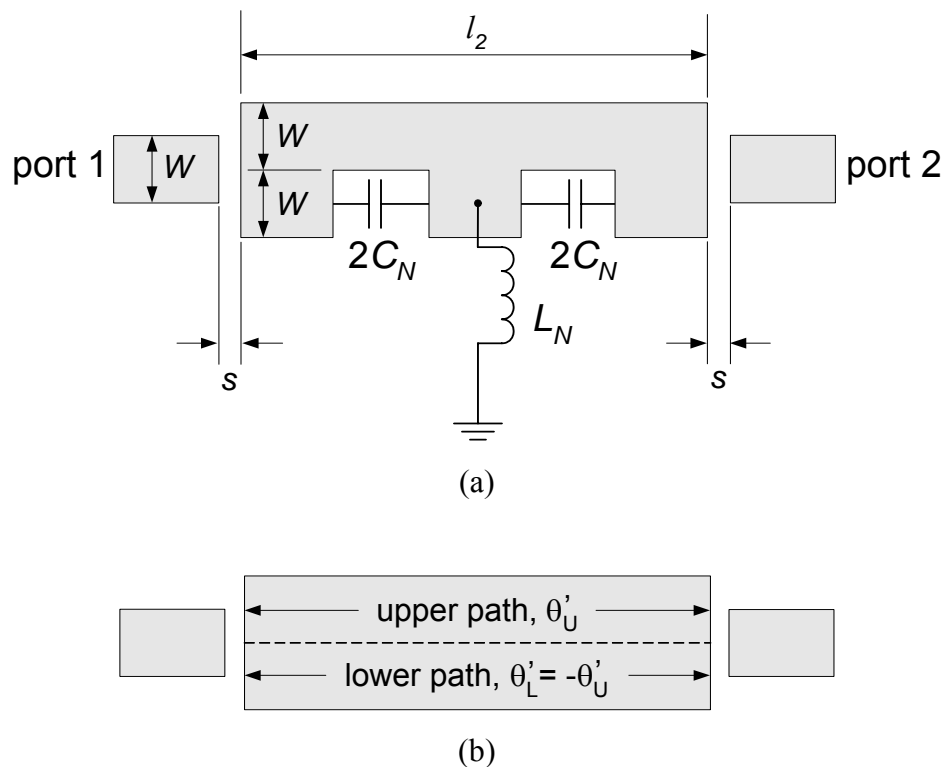


Fig. 45 (a) Layout and (b) condition for resonance for ring resonator with an inner diameter of zero using an NRI TL section

The proposed NRI ring resonators shown in Figs. 44 and 45 are designed for a resonant frequency of 1.2 GHz. Both are fabricated on 0.508 mm (20 mil) thick

RT/Duroid 5870 substrate with a relative dielectric constant of 2.33. The chip components include Panasonic surface mount capacitors (1.0×0.5 mm) of value $2C_N = 12$ pF and inductors (1.6×0.8 mm) of value $L_N = 15$ nH. The dimensions of the resonator with an inner diameter greater than zero as shown in Fig. 44 are $l_1 = 6.2$ mm, $W = 1.47$ mm, and $d = 1.02$ mm. The dimensions of the resonator with an inner diameter of zero as shown in Fig. 45 are $l_2 = 6.93$ mm and $W = 1.47$ mm. The coupling gap spacing for both resonators is $s = 0.2$ mm.

Measurements are made using an Agilent 8510C network analyzer and the results are shown in Fig. 46. The measured responses of the proposed resonators are almost identical. The loaded Q for both resonators is about 48, which approximately equals the Q for the lumped inductor at 1.2 GHz. Therefore, if the design requires a higher Q, a lower loss inductor can be used. At 1.2 GHz, the proposed resonator offers 6 dB lower insertion loss (for the same gap spacing) and has a maximum dimension 32% more compact than the gap coupled NRI line resonator presented previously. Compared to a conventional half-wavelength ring resonator at 1.2 GHz, the total circumference of the proposed resonator (including both upper and lower paths) is reduced by 84%. As expected, there are no higher-order resonances as in the conventional ring resonator.

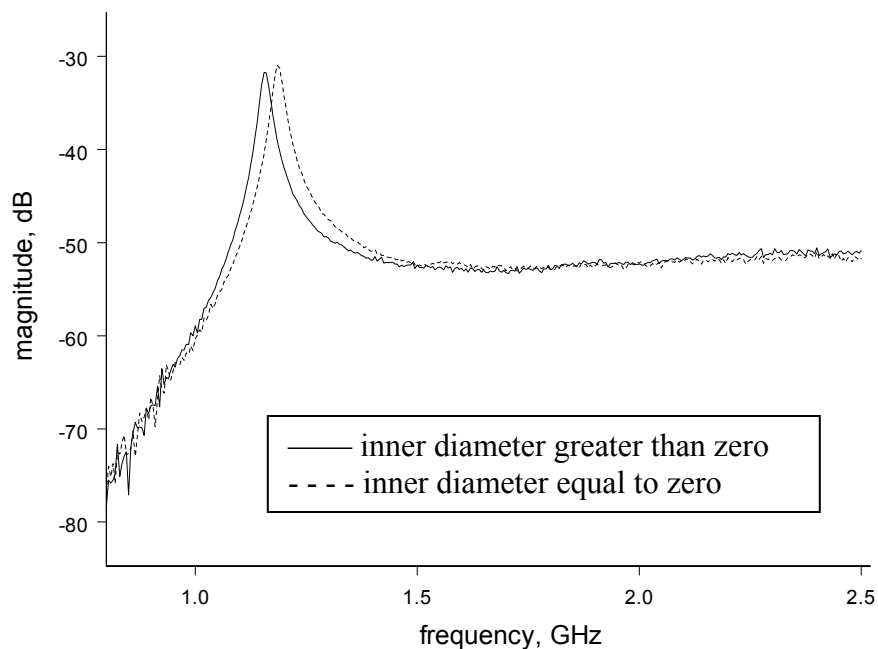


Fig. 46 Measured results for proposed ring resonators

D. Conclusions

In this chapter, the concepts related to negative refractive index technology and techniques were reviewed and applied to the design of compact microwave resonators. The compact NRI line resonator was found to be 86% more compact than that of the conventional one. Furthermore, the maximum dimension of the NRI ring resonator was 32% more compact than that of the NRI line resonator. It is also demonstrated that the ring resonator resonates even with an inner diameter of zero. Additionally, both the line and ring NRI resonators presented herein suppress higher order resonances (harmonics).

CHAPTER IV

SUMMARY AND RECOMMENDATIONS FOR FUTURE STUDY

A. Summary

Modern RF and microwave wireless systems usually require circuit minimization, which leads to cost reduction. Hence, size reduction is a major design consideration for practical applications. This thesis covers two separate topics in which both contribute the area compact microwave circuit design.

The first topic involves determining the distance that post production tuning bars should be from the microstrip thru line to cause a negligible effect when they are not used. To nullify the parasitic effects of the tuning bars, conventional wisdom suggests placing the bars 1.0 to 1.5 substrate heights away from the main line. This thesis puts this conventional wisdom to the test by systematically analyzing the error attributable to common GaAs MMIC and alumina/Ferro A6M TFN tuning bar configurations for a range of offset distances. The analysis was carried out primarily using a commercially available, numerical electromagnetic simulator due to its accuracy, practicality, and adaptability to the various tuning bar geometries. Distance-from-the-line curves as well as recommended offset distances are provided to facilitate the tuning bar placement with minimum parasitic effects on the circuit. It turns out that the conventional offset distance of 1.0 to 1.5 substrate heights is rather conservative for many cases, and therefore does not result in the most efficient and cost-effective placement of the tuning bars. In fact, negligible coupling exists at offset distances between 0.5-0.7 substrate heights for many configurations.

Also in this thesis, subwavelength line and ring resonators using an NRI TL section have been realized. Resonance occurs when the effective length of the loaded TL equals zero degrees. The advantages of the new resonators over their conventional counterparts include both considerable size reduction and harmonic suppression. It is expected that the new resonators will find new applications in the design of compact microstrip filters and oscillators.

B. Recommendations for Future Study

The tuning bar configurations, dimensions, and substrates analyzed in this thesis were specified by Raytheon Company. It is therefore recommended that other common tuning bar configurations and parameters be examined, so that a more comprehensive list of recommended offset distances can be tabulated and available to the circuit designer. Additionally, for certain applications, power efficient MEMs switches could be used instead of bond wire to connect the thru line to the tuning chip. To determine the parasitic effects on circuit performance, this requires a study of the coupling between the open MEMs switch and tuning bar.

Another area that deserves future study is the use of the proposed NRI resonators for practical applications including filters or oscillators. The small size of the resonators, alone, may lead to novel designs. For example, a conventional ring resonator could physically encircle one or more of the NRI ring resonators which may lead to new and compact cross-coupled filters.

REFERENCES

- [1] Sonnet Software, Inc. *Sonnet 8.52*, Liverpool, NY. 2002.
- [2] J.D. Guill "A Study of Microstrip T-Junction Discontinuity Effects and Modeling on GaAs Substrates". Masters Thesis, Department of Electrical Engineering. Texas A&M University. College Station. December 1999.
- [3] Zeland Software, Inc. *IE3D 10.02*, Fremont, CA. 2003.
- [4] Agilent Technologies, *Advanced Design System 2003A*, Palo Alto, CA.
- [5] Applied Wave Research. (June 2003). TX-Line 2001. [Online]. Available: <http://www.appwave.com/products/txline.html>.
- [6] Zeland Software, Inc., (June 2003). LineGauge Basic. [Online]. Available: <http://www.zeland.com/freeware.html>.
- [7] K. Chang, *RF and Microwave Wireless Systems*. New York: Wiley, 2000.
- [8] D.M. Pozar, *Microwave Engineering*, 2nd ed. New York: Wiley, 1998.
- [9] L. Brillouin, *Wave Propagation in Periodic Structures*, 2nd ed. New York: Dover, 1953.
- [10] J.-F. Kiang, *Novel Technologies for Microwave and Millimeter-Wave Applications*, Boston: Kluwer, 2004.
- [11] M.-K. Hu, D. Cheng, "A new class of artificial dielectrics," in *WESCON/58 Conf. Rec.*, vol. 2, Aug. 1958, pp.21-25.
- [12] D.R. Smith, W.J. Padilla, D.C. Vier, S.C. Nemat-Nasser, and S. Schultz, "Composite medium with simultaneously negative permeability and permittivity," *Phys. Rev. Lett.*, vol. 84, no. 18, pp. 4184-4187, 2000.
- [13] R.A. Shelby, D.R. Smith, and S. Schultz, "Experimental verification of a negative index of refraction," *Science*, vol. 292, pp. 77-79, 2001.
- [14] C.L. Holloway, E.F. Kuester, J. Baker-Jarvis, and P. Kabos, "A double negative (DNG) composite medium composed of magnetodielectric spherical particles embedded in a matrix," *IEEE Trans. Antennas Propogat.*, vol. 51, pp. 2596-2603, Oct. 2003.

- [15] G.V. Eleftheriades, A.K. Iyer, and P.C. Kremer, "Planar negative refractive index media using periodically L-C loaded transmission lines," *IEEE Trans. Microwave Theory Tech.*, vol. 50, pp. 2702-2712, Dec. 2002.
- [16] V.G. Veselago, "The Electrodynamics of substances with simultaneously negative values of ϵ and μ ," *Sov. Phys. Usp.*, vol 10, pp 509-514, Jan. 1968.
- [17] B. Szentpáli, "Metamaterials: A new concept in the microwave technique," *TELSIKS 2003*, vol. 1, pp. 127-132, Oct. 2003.
- [18] D.R. Smith, N. Kroll, "Negative Refractive Index in Left-Handed Materials," *Phys. Rev. Lett.*, vol. 85, no. 14, pp. 2933-2936, Oct. 2000.
- [19] J.B. Pendry, "Negative refraction makes a perfect lens," *Phys. Rev. Lett.*, vol. 85, no. 18, pp. 3966-3969, 2000.
- [20] J.B. Pendry, A.J. Holden, D.J. Robbins, and W.J. Stewart, "Magnetism from conductors and enhanced nonlinear phenomena," *IEEE Trans. Microwave Theory Tech.*, vol. 47, pp. 2075-2081, Nov. 1999.
- [21] ———, "Low-frequency plasmons in thin wire structures," *Phys. Condens. Matter*, vol. 10, pp. 4785-4809, 1998.
- [22] C. Caloz, H. Okabe, T. Iwai, and T. Itoh, "Transmission line approach of left-handed (LH) materials," *USNC/URSI National Radio Science Meeting*, San Antonio, TX, June 2002.
- [23] A.K. Iyer and G.V. Eleftheriades, "Negative refractive index metamaterials Supporting 2-D waves," *IEEE-MTT-S Int'l Symp. Digest*, pp. 1067-1070, Seattle, WA, June 2002.
- [24] L.I-Hsiang, C. Caloz, and T. Itoh, "A branch-line coupler with two arbitrary operating frequencies using left-handed transmission lines," *IEEE-MTT-S Int'l Symp. Digest*, pp. 325-328, June 2003.
- [25] H. Okabe, C. Caloz, and T. Itoh, "A compact enhanced-bandwidth hybrid ring using an artificial lumped-element left-handed transmission-line section," *IEEE Trans. Microwave Theory Tech.*, vol. 52, pp. 798-804, March 2004.

- [26] M. Anonniades, and G.V. Eleftheriades, "Compact linear lead/lag metamaterial phase shifters for broadband applications," *IEEE Antennas Wireless Propagat. Lett.*, vol. 2, pp. 103-106, 2003.
- [27] A. Grbic and G.V. Eleftheriades, "Periodic analysis of a 2-D negative refractive index transmission line structure," *IEEE Trans. Antennas Propogat.*, vol. 51, pp. 2604-2611, Oct. 2003.
- [28] A. Sanada, C. Caloz, T. Itoh, "Planar distributed structures with negative refractive index," *IEEE Trans. Microwave Theory Tech.*, vol. 52, pp. 1252-1263, April 2004.
- [29] A. Grbic and G.V. Eleftheriades, "Experimental verification of backward-wave radiation from a negative refractive index metamaterial," *J. Appl. Phys.*, vol. 92, no. 10, pp. 5930-5935, Nov. 2002.
- [30] C. Caloz, A. Sanada, T. Itoh, "A novel composite right-/left-handed coupled-line directional coupler with arbitrary coupling level and broad bandwidth," *IEEE Trans. Microwave Theory Tech.* vol. 52, pp. 980-992, March 2004.
- [31] S. Ramo, J.R. Whinnery, and T. Van Duzer, *Fields and Waves in Communication Electronics*, 3rd ed. New York: Wiley, 1994.
- [32] J.C. Slater, *Microwave Electronics*, Princeton, NJ: D. Van Nostrand and Co. 1950.
- [33] R. Chatterjee, *Elements of Microwave Engineering*, New York: Wiley, 1986.
- [34] S. Sudhakaran, Y. Han, C.G. Parini, "An experimental verification of spatial harmonics on negative refraction," *IEEE-AP-S Symp. Digest*, vol. 4, pp. 3757-3760, June 2004.
- [35] R.E. Collin, F.J. Zucker, *Antenna Theory Part 2*, New York: McGraw-Hill, 1969.
- [36] N. Engheta, "An idea for thin subwavelength cavity resonators using metmaterials with negative permittivity and permeability," *IEEE Antennas Wireless Propagat. Lett.*, vol. 1, pp. 10-13, 2002.

- [37] A.D. Scher, C.T. Rodenbeck, K. Chang, "Compact gap coupled resonator using negative refractive index microstrip line," *Electron. Lett.*, vol. 40, pp. 126-127, Jan. 2004.

APPENDIX A
MATLAB CODE FOR GENERATING NRI TL DISPERSION
DIAGRAM

```

%nri_tl_displot.m
%Purpose: To calculate and plot the dispersion diagram of a lossless NRI TL
% unit cell.

LN=0.01*10^-9; %Lumped element inductance (H)
CN=1*10^-12; %Lumped element capacitance (F)
Z0=20; %Host TL characteristic impedance (Ohms)
TL_beta_d_at_operating_freq=10; %Host TL electrical length (Degrees)
operating_freq=1*10^9; %Operating Frequency for TL_beta_d (Hz)
freq=(0.01:.005:9)*10^9; %Frequency range to plot (Hz)

%Determine host TL propagation constant over frequency range of interest:
freq=transpose(freq);
TL_beta_d=(pi/180)*(TL_beta_d_at_operating_freq/operating_freq)*freq;

%RHS of dispersion relation:
arg=cos(TL_beta_d).*(1-1./(4*(2*pi)^2*(freq).^2*LN*CN))...
    +sin(TL_beta_d).*(1./(2*2*pi*freq*CN*Z0)+Z0./(2*2*pi*freq*LN))...
    -1./(4*(2*pi)^2*(freq).^2*LN*CN);

NRI_beta_d=acos(arg); %Solve dispersion equation
freq=freq/10^9; %Convert frequency to GHz

%Determine which data points are real (propagating) or imaginary (stop
%band) and store this information in an array called 'immatrix':
immatrix=0;
for n=1:size(NRI_beta_d)
    immatrix(n,1)=isreal(NRI_beta_d(n));
end

sizeofdataset=size(freq);
if immatrix(sizeofdataset(1,1))==1 & immatrix(1,1)==1
    casenum=1; %if both first and last number in betad is real we have case #1.
elseif immatrix(sizeofdataset(1,1))==1 & immatrix(1,1)==0
    casenum=2; %if first number in betad is imaginary and last number is real we have
    %case #2.
elseif immatrix(sizeofdataset(1,1))==0 & immatrix(1,1)==1
    casenum=3; %if first number in betad is real and last number is immaginary we have
    %case #3.
elseif immatrix(sizeofdataset(1,1))==0 & immatrix(1,1)==0
    casenum=4; %if both first and last number in betad is immaginary we have case #4.
end

plotpnts=[]; %The matrix 'plotpnts' will contain the range of points (real beta_d) to plot.

```

```

if casenum==1 | casenum==3
    plotpnts(1)=1 ; %Since the first number is real in cases 1 and 2, we start plotting from
    %this point.
end

for n=2:sizeofdataset(1,1)-1
    sizepp=size(plotpnts);
    if immatrix(n,1)==0 & immatrix(n-1,1)==1 %Get point of transition from real to
    %imaginary
        plotpnts(sizepp(1,1)+1,1)=n-1;
    end
    if immatrix(n,1)==1 & immatrix(n-1,1)==0 %Get point of transition from imaginary to
    %real
        plotpnts(sizepp(1,1)+1,1)=n;
    end
end
sizepp=size(plotpnts); %Update size of 'plotpnts'

if casenum==1 | casenum==2
    plotpnts(sizepp(1,1)+1,1)=sizeofdataset(1,1); %Since the last number is real in cases
    %1 and 2 we plot up to this point
end

sizepp=size(plotpnts); %Update size of 'plotpnts'
clf; close; %clears and closes current figures
hold on; %enables multiple plots in same figure

for n=1:2:sizepp(1,1) %plot for positive beta_d
    plot(NRI_beta_d(plotpnts(n,1):plotpnts(n+1,1)),...
        freq(plotpnts(n,1):plotpnts(n+1,1)),...
        'k','LineWidth',2)
end
for n=1:2:sizepp(1,1) %plot for negative beta_d
    plot(-NRI_beta_d(plotpnts(n,1):plotpnts(n+1,1)),...
        freq(plotpnts(n,1):plotpnts(n+1,1)),...
        'k','LineWidth',2)
end

box on
axis([-pi,pi,0,max(freq)])
ylabel('Frequency (GHz)')
xlabel('\beta_B_1_o_c_hd (radians)')
set(gca,'XTick',-pi:pi/2:pi)
set(gca, 'xticklabel', '-p | -p/2 | 0 | p/2 | p', 'fontname','symbol');

```


VITA

Aaron David Scher was born in Seattle, Washington on May 27, 1981. In May of 2003 he received a Bachelor of Science degree in electrical engineering summa cum laude from Texas A&M University in College Station, Texas. Subsequently, he started his M.S. degree in electrical engineering at Texas A&M University under the direction of Dr. Kai Chang in the Electromagnetics and Microwave Laboratory. He spent the summer of 2004 working at Southwest Research in San Antonio, Texas at their Signal Exploitation and Geolocation Division. During the spring of 2005, he was a teaching assistant which involved teaching the laboratory section of an undergraduate electric circuit theory class. Aaron's permanent address is: 4501 Michelle Dr. Arlington, TX 76016.